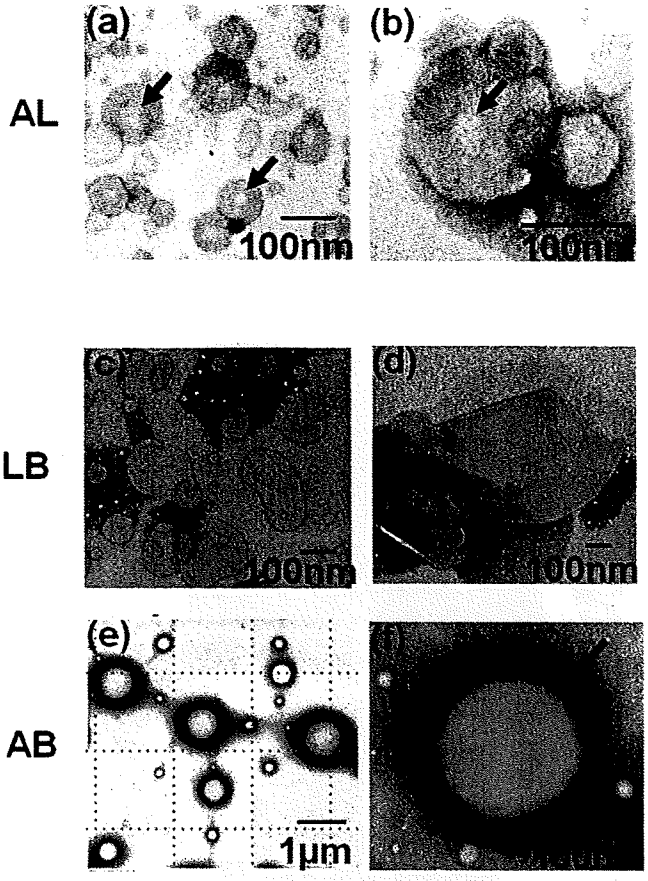

Fig. 3. Three types of ultrasound contrast agent from negative staining. AL: (a) ×50 000, (b) ×100 000. LB: (c) ×15 000, (d) ×10 000. AB: (e) ×3500, (f) ×20 000. The black arrows in (a) and (b) show where electron density was relatively low, indicating the presence of gas. The black arrow in (f) indicates albumin in filament form. (a)–(f) were stained at room temperature. (a), (b) JEOL JEM2000EX operated at 100 kV. (c)–(f) H-7600 operated at 80 kV.

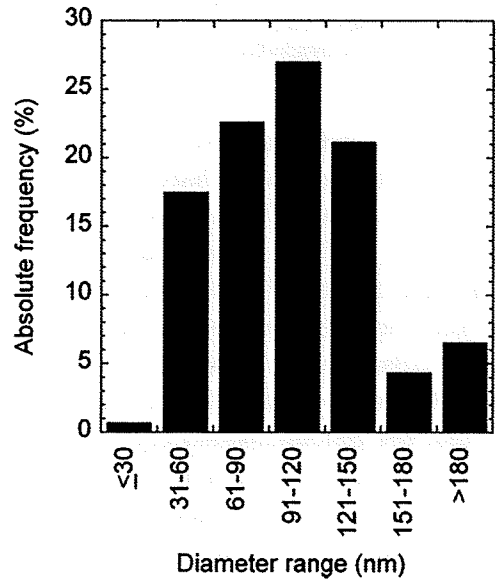

Fig. 4. Histogram of the absolute frequency distribution. The data were obtained from 10 TEM images. The maximum value was obtained within the class interval of 91–120 nm.

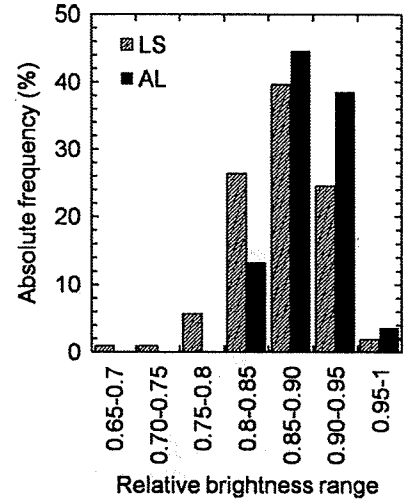

Fig. 5. Relative brightness range. AL and LS TEM micrographs were analyzed to assess the average brightness value of the inside of each kind of liposome. The inner area of each liposome image was digitally selected to measure its mean brightness value. Relative brightness values (measured mean brightness/background brightness) were obtained for 106 LSs and 83 ALs. The statistical distribution of ALs is slightly shifted to relative brightness values closer to 1 compared to the distribution of LSs, indicating that gas bubbles are actually present inside some of the ALs.

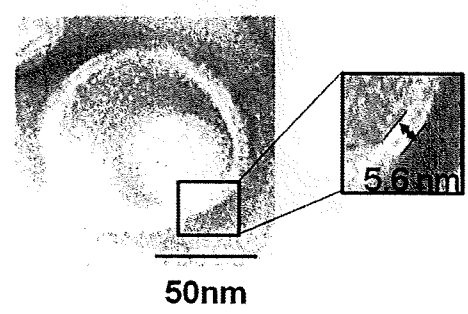

Fig. 6. Shell structure of AL. TEM micrograph of AL, negatively stained at 80°C. The distance between two lines in the magnified figure was 5.6 nm, indicating a single lipid bilayer. Original magnification, ×50 000. JEOL JEM2000EX operated at 100 kV.

AL was 24% (17 out of 70 liposomes). This value was similar to the 20% obtained and illustrated in Fig. 3a and b. Figure 7b shows that some ALs have an equal volume occupied by liquid and gas. The white arrows indicate the outside boundary, while the black arrows indicate the inside boundary. G shows the presence of gas, and L the presence of liquid. It is hard to judge whether the interface between the gas and the liquid within the AL is a gas/liquid interface or a lipid interface. Figure 7c shows an AL primarily occupied by gas. The proportion of gas relative to liquid is likely to vary depending on how the cross-section is cut. Figure 7d shows a liposome which was not sonicated, with a liquid-filled inside.

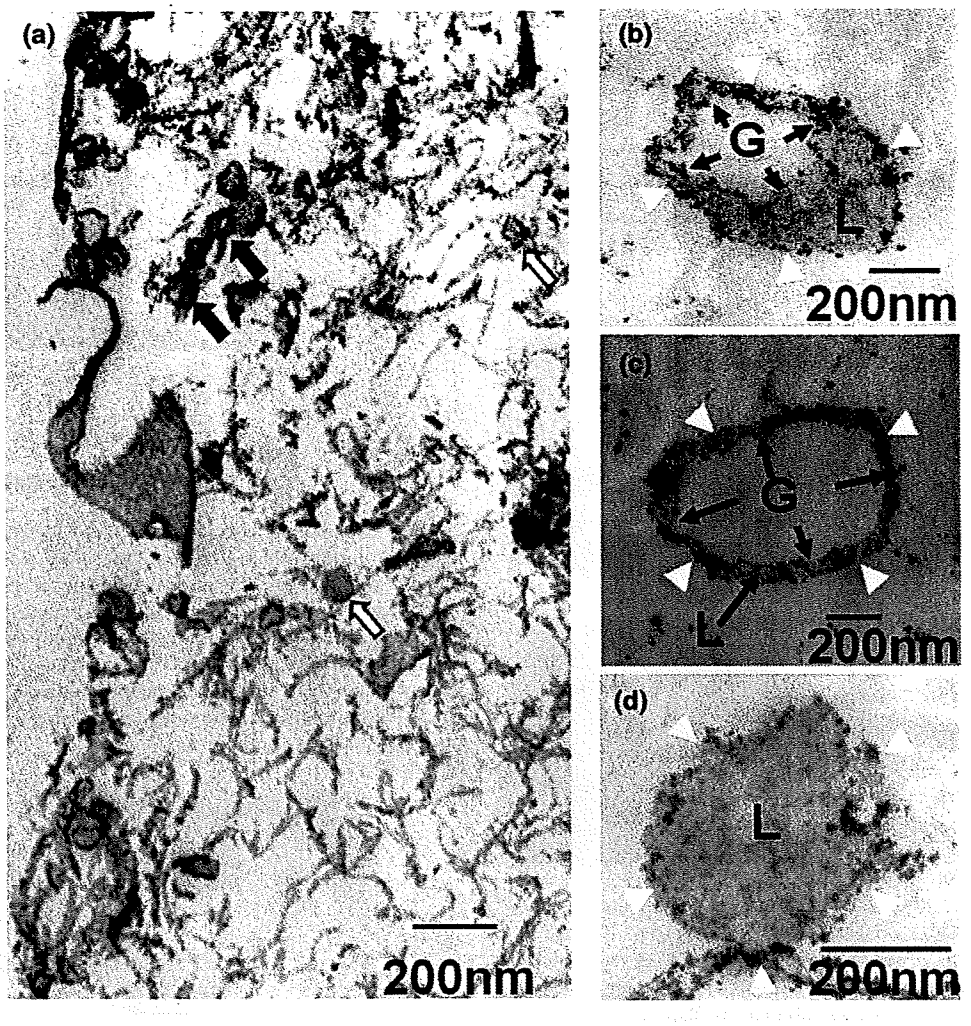

Fig. 7. Structure of AL from double staining. (a) The black arrows indicate the presence of gas in AL, while the white arrow indicates liquid. Original magnification: ×20 000. (b) AL occupied by ~50% (v/v) gas (G) and 50% (v/v) liquid (L). The white arrows indicate the outside boundary, while the black arrows indicate the inside boundary. Original magnification: ×30 000. (c) AL occupied mainly by gas (G). The liquid (L) portion was small. The white arrow indicates the outside boundary, while the black arrow indicates the inside boundary. Original magnification: ×20 000. (d) Liposome, which was not sonicated. The inside was filled with liquid (L). The white arrows indicate the outside boundary. Original magnification: ×50 000. (a)–(d) were obtained with JEOL JEM2000EX operated at 100 kV.

Discussion

The structure of an AL was investigated using TEM, and was compared with that for LB and AB. First we measured the diameter of AL by dynamic light scattering. The diameter of AL was ~200 nm (Table 1), which was about double the diameter calculated from the analysis of 10 TEM micrographs (Fig. 4). With dynamic light scattering, the size was measured immediately after AL production. TEM measurement indicated that the size of AL may have been influenced by the staining process and repeated electron beam exposure. These external factors might shift the frequency distribution to the lower value.

The zeta potential was derived from the hypothesis that ALs, LBs and ABs are hard particles [15]. ALs and LBs were found to be almost neutral, whereas AB had strong negative values (Table 1). As can be seen in TEM images (Fig. 3e and f), the electron beams were strongly scattered around the shell surface of the ABs. The key component of AB, albumin, was detected in its filament form. Ohshima [15] reported that the Smoluchowski equation cannot be applied to soft particles such as red blood cells, i.e. particles with an electric surface charge boundary in which a slip line exists. ABs are most likely to be a type of soft particle, for which this equation cannot be applied. Equations taking into account the properties of this kind of particles should be investigated.

From negative staining observations, it was assumed that AL have a single lipid bilayer as a shell structure (Fig. 6). The percentage of AL in which the presence of gas was detected was ~20%, and the proportion of volume occupied by gas and liquid varied depending on how the cross-sections were cut. Although it was hard to quantify the percentage of gas occupying the interior of AL due to the limited number of TEM images, it was clear from echogenicity that the C_3F_8 gas was actually encapsulated in ALs (Figs. 2 and 5).

Several acoustic liposome structures have been suggested [17,18]. Huang *et al.* [17] proposed that the internal volume was occupied by air and liquid compartments, and that the interface between the air and liquid compartments was a lipid monolayer. Suzuki *et al.* [18] suggested that both liquid and unilamellar lipids containing air were encapsulated by a single lipid bilayer. In the present study, we observed that gas and liquid seemed to be encapsulated together by a single lipid bilayer. However, we could not judge whether the interface between the gas and the liquid was the gas/liquid interface or the lipid interface.

The co-existence of gas and liquid in ALs provides evidence of its echogenicity and drug-carrying capabilities. Further, the tissue specificity of ALs can be improved by conjugating ligands against the target tissue with PEG on the AL surface. Recently, a high-frequency ultrasound system with ALs has been developed and applied so far to the imaging of anterior segment of the eye [19], skin [20] and tumor vasculature [21]. Studies have shown that the permeability of the tumor vasculature is enhanced, and the phenomenon is recognized as the EPR effect [11].

Most anticancer drugs have diameters of 10–120 nm: Genexol-PM (20–50 nm in diameter), Doxil (80–90 nm in diameter), Abraxane (120 nm in diameter) [12]. Sonoporation delivery efficiency, *in vivo* behavior and tissue-specificity of ALs would possibly be enhanced if the diameter was controlled within the range of 10–120 nm, the surface was positively or negatively charged, and ligands against the tumor were conjugated to PEG on the surface [22–24].

Concluding remarks

In summary, the findings of the present study indicate that AL have a shell consisting of a single lipid bilayer and can encapsulate both drugs and gas. The PEG distributed over the surface can be conjugated with tissue-specific ligands. Developing functional AL will assure the effectiveness of sonoporation.

Funding

This work was supported by a Grant-in-Aid for Scientific Research (B) [20300173 to T.K., 19390507 to S.M.]; a Grant-in-Aid for Scientific Research on Priority Area, MEXT [20015005 to T.K.]; a Grant for Research on Advanced Medical Technology, the Ministry of Health, Labor and Welfare of Japan [H19-nano-010 to T.K.]; a Grant for Research on Development of Systems and Technology for Advanced Measurement and Analysis, JST [T.K.]; and a Grant-in-Aid for JSPS Fellows [21-7271 to S.H.].

Acknowledgements

The authors would like to thank Yukiko Watanabe, Rui Chen and Li Li, for their technical assistance.

References

1 Kodama T, Tomita Y, Koshiyama K, and Blomley M J (2006) Transfection effect of microbubbles on cells in superposed ultrasound waves and behavior of cavitation bubble. *Ultrasound Med. Biol.* **32**: 905–914.

2 Lindner J R (2004) Microbubbles in medical imaging: current applications and future directions. *Nat. Rev. Drug Discov.* **3**: 527–532.

3 Shohet R V, Chen S, Zhou Y T, Wang Z, Meidell R S, Unger R H, and Grayburn P A (2000) Echocardiographic destruction of albumin microbubbles directs gene delivery to the myocardium. *Circulation* **101**: 2554–2556.

4 Christiansen J P, French B A, Klibanov A L, Kaul S, and Lindner J R (2003) Targeted tissue transfection with ultrasound destruction of plasmid-bearing cationic microbubbles. *Ultrasound Med. Biol.* **29**: 1759–1767.

5 Suzuki R, Takizawa T, Negishi Y, Utoguchi N, Sawamura K, Tanaka K, Namai E, Oda Y, Matsumura Y, and Maruyama K (2008) Tumor specific ultrasound enhanced gene transfer *in vivo* with novel liposomal bubbles. *J. Control. Release* **125**: 137–144.

6 Suzuki R, Oda Y, Utoguchi N, Namai E, Taira Y, Okada N, Kadowaki N, Kodama T, Tachibana K, and Maruyama K (2009) A novel strategy utilizing ultrasound for antigen delivery in dendritic cell-based cancer immunotherapy. *J. Control. Release* **133**: 198–205.

7 Church C C (1995) The effrcts of an elastic solid-surface layer on the radial pulsations of gas-bubbles. *J. Acoust. Soc. Am.* **97**: 1510–1521.

8 Kodama T, Tomita Y, Watanabe Y, Koshiyama K, Yano T, and Fujikawa S (2009) Cavitation bubbles mediated molecular delivery during sonoporation. *J. Biomech. Sci. Eng.* **4**: 124–140.

9 Suzuki R, Takizawa T, Negishi Y, Hagisawa K, Tanaka K, Sawamura K, Utoguchi N, Nishioka T, and Maruyama K (2007) Gene delivery by combination of novel liposomal bubbles with perfluoropropane and ultrasound. *J. Control. Release* **117**: 130–136.

10 Klibanov A L, Maruyama K, Torchilin V P, and Huang L (1990) Amphipathic polyethyleneglycols effectively prolong the circulation time of liposomes. *FEBS Lett.* **268**: 235–237.

11 Matsumura Y and Maeda H (1986) A new concept for macromolecular therapeutics in cancer chemotherapy: mechanism of tumoritropic

accumulation of proteins and the antitumor agent smancs. *Cancer Res.* **46**: 6387–6392.

12 Davis M E, Chen Z G, and Shin D M (2008) Nanoparticle therapeutics: an emerging treatment modality for cancer. *Nat. Rev. Drug Discov.* **7**: 771–782.

13 Aoi A, Watanabe Y, Mori S, Takahashi M, Vassaux G, and Kodama T (2008) Herpes simplex virus thymidine kinase-mediated suicide gene therapy using nano/microbubbles and ultrasound. *Ultrasound Med. Biol.* **34**: 425–434.

14 Watanabe Y, Aoi A, Horie S, Tomita N, Mori S, Morikawa H, Matsumura Y, Vassaux G, and Kodama T (2008) Low-intensity ultrasound and microbubbles enhance the antitumor effect of cisplatin. *Cancer Sci.* **99**: 2525–2531.

15 Ohshima H (1994) Eectrophoretic mobility of soft particles. *J. Colloid Interface Sci.* **163**: 474–483.

16 Yanai H (2007) *Statcel—The Useful Add-in Forms on Excel.* (OMS, Tokyo).

17 Huang S L, and Macdonald R C (2004) Acoustically active liposomes for drug encapsulation and ultrasound-triggered release. *Biochim. Biophys. Acta* **1665**: 134–141.

18 Suzuki R, Takizawa T, Negishi Y, Utoguchi N, and Maruyama K (2008) Effective gene delivery with novel liposomal bubbles and ultrasonic destruction technology. *Int. J. Pharm.* **354**: 49–55.

19 Pavlin C J, and Foster F S (1998) Ultrasound biomicroscopy. High-frequency ultrasound imaging of the eye at microscopic resolution. *Radiol. Clin. North Am.* **36**: 1047–1058.

20 Vogt M, and Ermert H (2008) Limited-angle spatial compound imaging of skin with high-frequency ultrasound (20 MHz). *IEEE Trans. Ultrason. Ferroelectr. Freq Control* **55**: 1975–1983.

21 Lyshchik A, Fleischer A C, Huamani J, Hallahan D E, Brissova M, and Gore J C (2007) Molecular imaging of vascular endothelial growth factor receptor 2 expression using targeted contrast-enhanced high-frequency ultrasonography. *J. Ultrasound Med.* **26**, 1575–1586.

22 Schneider M (2008) Molecular imaging and ultrasound-assisted drug delivery. *J. Endourol.* **22**: 795–802.

23 Kaufmann B A, and Lindner J R (2007) Molecular imaging with targeted contrast ultrasound. *Curr. Opin. Biotechnol.* **18**: 11–16.

24 Palmowski M, Huppert J, Hauff P, Reinhardt M, Schreiner K, Socher M A, Hallscheidt P, Kauffmann G W, Semmler W, and Kiessling F (2008) Vessel fractions in tumor xenografts depicted by flow- or contrast-sensitive three-dimensional high-frequency Doppler ultrasound respond differently to antiangiogenic treatment. *Cancer Res.* **68**: 7042–7049.

Journal of Controlled Release 133 (2009) 198–205

Contents lists available at ScienceDirect

Journal of Controlled Release

journal homepage: www.elsevier.com/locate/jconrel

A novel strategy utilizing ultrasound for antigen delivery in dendritic cell-based cancer immunotherapy

Ryo Suzuki [a], Yusuke Oda [a], Naoki Utoguchi [a], Eisuke Namai [a], Yuichiro Taira [a], Naoki Okada [b], Norimitsu Kadowaki [c], Tetsuya Kodama [d], Katsuro Tachibana [e], Kazuo Maruyama [a,*]

[a] Department of Biopharmaceutics, School of Pharmaceutical Sciences, Teikyo University, 1091-1 Suwarashi, Sagamiko-cho, Sagamihara, Kanagawa 229-0195, Japan
[b] Department of Biotechnology and Therapeutics, Graduate School of Pharmaceutical Sciences, Osaka University, 1-6 Yamadaoka, Suita, Osaka 565-0871, Japan
[c] Department of Hematology and Oncology, Graduate School of Medicine, Kyoto University, 54 Shogoin Kawara-cho, Sakyo-ku, Kyoto 606-8507, Japan
[d] Department of Biomedical Engineering, Graduate School of Biomedical Engineering, Tohoku University, 2-1 Seiryo-machi, Aoba-ku, Sendai 980-8575, Japan
[e] Department of anatomy, School of medicine, Fukuoka University, 7-45-1 Nanakuma, Jonan-ku, Fukuoka 814-0180, Japan

ARTICLE INFO

Article history:
Received 12 August 2008
Accepted 16 October 2008
Available online 31 October 2008

Keywords:
Dendritic cells
Antigen delivery system
Cancer immunotherapy
Ultrasound
Liposomes

ABSTRACT

In dendritic cell (DC)-based cancer immunotherapy, it is important that DCs present peptides derived from tumor-associated antigens on MHC class I, and activate tumor-specific cytotoxic T lymphocytes (CTLs). However, MHC class I generally present endogenous antigens expressed in the cytosol. We therefore developed an innovative approach capable of directly delivering exogenous antigens into the cytosol of DCs; i.e., a MHC class I-presenting pathway. In this study, we investigated the effect of antigen delivery using perfluoropropane gas-entrapping liposomes (Bubble liposomes, BLs) and ultrasound (US) exposure on MHC class I presentation levels in DCs, as well as the feasibility of using this antigen delivery system in DC-based cancer immunotherapy. DCs were treated with ovalbumin (OVA) as a model antigen, BLs and US exposure. OVA was directly delivered into the cytosol but not via the endocytosis pathway, and OVA-derived peptides were presented on MHC class I. This result indicates that exogenous antigens can be recognized as endogenous antigens when delivered into the cytosol. Immunization with DCs treated with OVA, BLs and US exposure efficiently induced OVA-specific CTLs and resulted in the complete rejection of E.G7-OVA tumors. These data indicate that the combination of BLs and US exposure is a promising antigen delivery system in DC-based cancer immunotherapy.

1. Introduction

Dendritic cells (DCs), which are unique antigen-presenting cells capable of priming naive T cells, are promising vaccine carriers for cancer immunotherapy [1]. To induce efficiently a tumor-specific cytotoxic T-lymphocyte (CTL) response, DCs should abundantly present epitope peptides derived from tumor-associated antigens (TAAs) via major histocompatibility complex (MHC) class I molecules [2]. In general, the majority of peptides presented via the MHC class I molecules are generated from endogenously synthesized proteins that are degraded by the proteasome [3]. On the other hand, exogenous antigens such as TAAs for DCs are preferentially presented on MHC class II molecules [3]. In order to prime efficiently TAAs specific for CTLs, it is important to develop a novel antigen delivery system, which can induce MHC class I restricted TAA presentation on DCs. Several researchers are developing antigen delivery tools based on the cross presentation theory of exogenous antigens for DCs [4–8]. In these studies, various types of antigen delivery carriers such as liposomes [6,7], poly(γ-glutamic acid) nanoparticles [5] and cholesterol pullulan nanoparticles [8], all of which can deliver antigen into DCs via the endocytosis pathway, have been developed. We have reported that IgG modified liposomes with entrapped antigen can induce cross presentation of exogenous antigen for DCs on MHC class I molecules [9]. These carriers deliver antigens into DCs via an endocytosis mechanism, with delivery thought to be due to exogenous antigen leaking from the endosome into the cytosol. It is therefore important to design an antigen delivery system which does not rely on the endocytosis pathway. In other study, it was reported that DCs pulsed with exogenous antigens by electroporation presented their antigens on MHC class I molecules and resulted

Abbreviations: Alexa-OVA, Alexa Fluor 488-conjugated ovalbumin; BL, Bubble liposome; CTL, cytotoxic T lymphocyte; DC, dendritic cell; DSPC, 1,2-distearoyl-sn-glycero-phosphatidylcholine; DSPE-PEG(2k)-OMe, 1,2-distearoyl-sn-glycero-3-phosphatidyl-ethanolamine-methoxypolyethyleneglycol; ER, endoplasmic reticulum; FBS, fetal bovine albumin; HLA, human leukocyte antigen; MHC, major histocompatibility complex; MTT, 3-(4,5-s-dimethylthiazol-2-yl)-2,5-diphenyl tetrazolium bromide; NaN_3, sodium azide; OVA, ovalbumin; PBS, phosphate buffer saline; US, ultrasound; TAA, tumor associated antigen.

* Corresponding author. Department of Biopharmaceutics, School of Pharmaceutical Sciences, Teikyo University, 1091-1 Suwarashi, Sagamiko-cho, Sagamihara, Kanagawa 229-0195, Japan. Tel.: +81 42 685 3722; fax: +81 42 685 3432.
E-mail address: maruyama@pharm.teikyo-u.ac.jp (K. Maruyama).

0168-3659/$ – see front matter © 2008 Elsevier B.V. All rights reserved.
doi:10.1016/j.jconrel.2008.10.015

in inducing MHC class I-mediated antitumor immunity. Although electroporation is commonly utilized as gene delivery method and deliver gene such as DNA and RNA into cytosol, Kim K.W. et al and Weiss J.M. et al. apply this system to antigen delivery into DCs [10,11]. Their reports also demonstrate the importance of delivering exogenous antigens into cytosol of DCs to induce MHC class I presentation of the antigens.

It has been reported that ultrasound (US) increases the permeability of the plasma membrane, which encourages the entry of DNA into cells [12,13]. The first studies applying US for gene delivery used frequencies in the range of 20–50 kHz [12,14]. However, these frequencies, along with cavitation, are also known to induce tissue damage if not properly controlled [15–17]. To address this problem, many studies into using therapeutic US for gene delivery have used frequencies of 1–3 MHz, intensities of 0.5–2.5 W/cm^2 and a pulse-mode [18–20]. In addition, it was reported that the combination of therapeutic US and microbubble echo contrast agents could enhance gene transfection efficiency [21–27]. In this method, DNA is effectively and directly transferred into the cytosol. This system has been applied to deliver proteins into cells [28,29], but not yet to deliver antigens into DCs for the purpose of cancer immunotherapy. Previously, we developed novel liposomal bubbles containing nanobubbles of the US imaging gas, perfluoropropane [30–34] and suggested that these "Bubble liposomes" (BLs) might be used as novel non-viral gene delivery tools if combined with US exposure. In the case of DCs, the antigen delivered into the cytosol would present on MHC class I molecules and result in priming antigen-specific CTLs. In this study, we examined the effectiveness of BLs combined with US exposure to deliver antigen into DCs. In addition, the effectiveness of this antigen delivery system in DC-based cancer immunotherapy was assessed.

2. Materials and methods

2.1. Cells

T cell hybridoma CD8-OVA1.3 (a kind gift from Dr. C.V. Harding, Department of Pathology, Case Western Reserve University, Cleveland, OH, USA), a cell type that recognizes SIINFEKL:H-2K^b complexes [35], was cultured in Dulbecco's modified Eagle's medium (DMEM, Sigma Chemical Co., St. Louis, MO, USA) supplemented with 10% heat inactivated fetal bovine serum (FBS, GIBCO, Invitrogen Co., Carlsbad, CA, USA), 50 μM 2-mercaptethanol (2-ME), 250 μg/ml amphotericin B (Wako Pure Chemical Industries, Ltd., Osaka, Japan) and 50 μg/ml gentamycin (Wako Pure Chemical Industries). EL-4 murine thymoma cells were cultured in RPMI 1640 supplemented with 10% FBS and 50 μM 2-ME. E.G7-OVA cells (OVA cDNA transfectant of EL4 cells) were maintained in RPMI 1640 supplemented with 10% FBS, 50 μM 2-ME and 400 μg/ml GENETICIN (G418 sulfate, GIBCO, Invitrogen). All culture media contained 50 U/ml penicillin and 50 μg/ml streptomycin (Wako Pure Chemical Industries).

2.2. Generation of mouse bone marrow-derived DCs

DCs were generated from bone marrow cells as described elsewhere [36]. Briefly, bone marrow cells were isolated from C57BL/6 mice and were cultured in RPMI 1640 with 10% FBS, 50 U/ml penicillin, 50 μg/ml streptomycin and 40 ng/ml mouse granulocyte-macrophage colony-stimulating factor (GM-CSF). After 8–16 days of culture, non-adherent cells were collected and used as DCs.

2.3. Preparation of BLs

Liposomes composed of 1,2-distearoyl-sn-glycero-phosphatidylcholine (DSPC) (NOF Corp., Tokyo, Japan) and 1,2-distearoyl-sn-glycero-3-phosphatidyl-ethanolamine-methoxypolyethyleneglycol (DSPE-PEG(2k)-OMe, (PEG Mw=ca. 2000), NOF) (94 : 6 (m/m)) were prepared by reverse phase evaporation. Briefly, all reagents (total lipid: 100 μmol) were dissolved in 8 ml of 1:1 (v/v) chloroform/diisopropyl ether, then 4 ml of phosphate buffered saline (PBS) was added. The mixture was sonicated and evaporated at 65 °C. The solvent was completely removed, and the size of the liposomes was adjusted to less than 200 nm using an extruding apparatus (Northern Lipids Inc., Vancouver, BC, Canada) and sizing filters (pore sizes: 100 and 200 nm; Nuclepore Track-Etch Membrane, Whatman plc, UK). After sizing, the liposomes were sterilized by passing them through a 0.45 μm pore size filter (MILLEX HV filter unit, Durapore PVDF membrane, Millipore Corp., MA, USA). The size of the liposomes was measured by dynamic light scattering (ELS-800, Otsuka Electronics Co., Ltd., Osaka, Japan). The average diameter of these liposomes was between 150–200 nm. Lipid concentration was measured using the Phospholipid C test (Wako Pure Chemical Industries). BLs were prepared from the liposomes and perfluoropropane gas (Takachiho Chemical Industrial Co., Ltd., Tokyo, Japan) [31,33]. Briefly, 5 ml sterilized vials containing 2 ml of the liposome suspension (lipid concentration: 2 mg/ml) were filled with perfluoropropane, capped, and then supercharged with 7.5 ml of perfluoropropane. The vial was placed in a bath-type sonicator (42 kHz, 100 W; BRANSONIC 2510J-DTH, Branson Ultrasonics Co., Danbury, CT, USA) for 5 min to form the BLs. In this method, the liposomes were reconstituted by sonication under the condition of supercharge with perfluoropropane in the 5 mL vial container. At the same time, perfluoropropane would be entrapped within lipids like micelles, which were made by DSPC and DSPE-PEG(2k)-OMe from liposome composition, to form nanobubbles. The lipid nanobubbles were encapsulated within the reconstituted liposomes, which sizes were changed into around 1 μm from 150–200 nm of original.

2.4. Antigen trafficking into DCs after antigen delivery with BLs and US exposure

Alexa Fluor 488 conjugated OVA (Alexa-OVA) was prepared with Alexa Fluor 488 succinimidyl ester (Molecular Probes, Invitrogen) according to the instruction manual. DCs (1×10^5 cells/ml) were cultured in a glass bottom dish (IWAKI, Asahi Glass Co. Ltd., Tokyo, Japan) overnight. After washing the cells with OptiMEM (Invitrogen), BLs (240 μg/ml) and Alexa-OVA (50 μg/ml) were added to the dish. Then, the DCs were exposed to US exposure (frequency: 2 MHz, duty: 10%, burst rate: 2.0 Hz, intensity 2.0 W/cm^2, time: 3×10 s (interval: 10 s)) using a Sonopore 4000 (6 mm diameter probe; Nepa Gene Co. Ltd., Chiba, Japan). This condition was decided referring to our reports about gene delivery [31,33] and Guo et al.'s report about the repeat US exposure with interval [37], and from the viewpoint of cytotoxicity for DCs. After US exposure, the DCs were incubated for 1 h at 37 °C, then washed with PBS, fixed with 3% paraformaldehyde for 10 min, and treated with 0.1% Triton X-100 (Wako Pure Chemical Industries) for 5 min. In addition, some DCs were washed with PBS, their nuclei were stained with propidium iodide (0.5 μg/ml) (Wako Pure Chemical Industries), and antigen trafficking was observed with a confocal laser microscope.

2.5. Antigen delivery following inhibition of the endocytosis pathway in DCs

DCs were pretreated with OptiMEM containing 10 mM NaN_3 for 1 h at 4 °C to inhibit the endocytosis pathway. After washing the cells, BLs (240 μg/ml) and Alexa-OVA (50 μg/ml) were added to the DCs in OptiMEM containing 10 mM sodium azide (NaN_3). The DCs were exposed to US exposure (frequency: 2 MHz, duty: 10%, burst rate: 2.0 Hz, intensity 2.0 W/cm^2, time: 3×10 s (interval: 10 s)), then washed with PBS containing10 mM NaN_3. After US exposure, DCs were fixed and their nuclei were stained as described above (2.4.).

2.6. Flow cytometry analysis of antigen delivery into DCs with BLs and US exposure

Alexa-OVA was delivered into DCs under inhibited endocytosis conditions as described above (2.5.). After washing, the DCs were stained with propidium iodide (100 ng/ml) and analyzed by flow cytometry (FACSCalibur, Becton, Dickinson and Company, Franklin Lakes, NJ, USA). In this study, living DCs (1×10^4 cells) were analyzed by gating out propidium iodide staining cells.

2.7. Assessment of MHC class I restricted OVA presentation

DCs (2.5×10^5 cells/500 μl/well (48-well plate)) were pulsed with OVA alone (0, 10, 100, 1000 μg/ml) or OVA (0, 10, 100, 1000 μg/ml) using US exposure (frequency: 2 MHz, duty: 10%, burst rate: 2.0 Hz, intensity 2.0 W/cm^2, Time: 3×10 s (interval: 10 s)) and/or BLs (240 μg/ml). After US exposure, the DCs were incubated for 1 h at 37 °C, then washed with PBS. After culturing for 24 h, the DCs were co-cultured for 20 h with T cell hybridoma CD8-OVA1.3 (2×10^5 cells/well) that recognizes SIINFEKL: H-2K^b complexes. The concentration of IL-2 in the supernatants was measured using an IL-2 ELISA Kit (BioSource International, Inc., Camarillo, CA, USA).

2.8. Assessment of cytotoxicity to DCs by the treatment of BLs and US exposure

DCs (2.5×10^5 cells/500 μl/well (48-well plate)) were treated with BLs (240 μg/ml) and/or US exposure (frequency: 2 MHz, duty: 10%, burst rate: 2.0 Hz, intensity 2.0 W/cm^2, Time: 3×10 s (interval: 10 s)). After US exposure, DCs were incubated for 1 h at 37 °C, and washed with PBS. The DCs were resuspended with cuture medium (250 μl) and cultured for 48 h. Cell viability was assayed using MTT (3-(4,5-s-dimethylthiazol-2-yl)-2,5-diphenyl tetrazolium bromide, Dojindo, Kumamoto, Japan) as described by Mosmann with minor modifications [38]. Briefly, MTT (5 mg/mL, 25 μL) was added to each well and the cells were incubated at 37 °C for 4 h. The formazan product was dissolved in 250 μL of 10% sodium dodecyl sulfate (SDS, Wako Pure Chemical Ind. Co., Ltd. Osaka, Japan) containing 15 mM HCl. Color intensity was measured using a microplate reader (POWERSCAN HT; Dainippon Pharmaceutical, Osaka, Japan) at test and reference wavelengths of 595 and 655 nm, respectively.

2.9. Immunization of mice with DCs and cytotoxicity assay

DCs (2.5×10^5 cells/500 μl/well) were pulsed with OVA alone (100 μg/ml) or OVA (100 μg/ml) using US exposure (frequency: 2 MHz, duty: 10%, burst rate: 2.0 Hz, intensity 2.0 W/cm^2, Time: 3×10 s (interval: 10 s)) and/or BLs (240 μg/ml) on a 48-well plate, then collected from 10 wells and seeded into 6-well plates. After 1 h incubation at 37 °C, the DCs were washed and cultured for 24 h at 37 °C. After washing, DCs (1×10^6 cells/100 μl) were intradermally injected into the backs of C57BL/6 mice. After 7 days, the mice were re-immunized. Seven days after the second immunization, splenocytes were obtained from five mice, and the splenocytes were pooled and stimulated with mitomycin C-treated E.G7-OVA cells at a ratio of 10:1 for 5 days. The stimulated splenocytes were used as effector cells for the cytotoxicity assay, using EL-4 or E.G7-OVA as the target cells in a flow cytometric assay employing two fluorochromes [39]. PKH-67, a fluorochrome which fluoresces green, binds to the cytoplasmic membrane and does not leak or transfer, was used to identify the target cell population. Propidium iodide fluoresces red and was used to detect non-viable cells. Use of these two fluorochromes and two parameter analyses allowed the identification of four subpopulations in the sample: live effectors, dead effectors, live targets and dead targets. By enumerating these subpopulations, the percent target lysis can be calculated.

2.10. Antitumor effect by prior immunization with antigen-pulsed DCs

DCs (2.5×10^5 cells/500 μl/well) were pulsed with OVA alone (100 μg/ml) or OVA (100 μg/ml) using US exposure (frequency: 2 MHz, duty: 10%, burst rate: 2.0 Hz, intensity 2.0 W/cm^2, Time: 3×10 s (interval: 10 s)) and/or BLs (240 μg/ml) on a 48-well plate, then collected from 10 wells and seeded into 6-well plates. After 1 h incubation at 37 °C, the DCs were washed and cultured for 24 h at 37 °C. After washing, the DCs (1×10^6 cells/100 μl) were intradermally immunized into the backs of C57BL/6 mice twice at intervals of one week. Seven days after the second immunization, E.G7-OVA cells (1×10^6 cells) were intradermally inoculated into the backs of mice and the size of the tumors was monitored using the formula: (major axis×minor axis^2)×0.5. All treated groups contained five mice.

2.11. Re-challenge of tumor cells

E.G7-OVA cells (1×10^6 cells) were injected into mice that were resistant to tumor cells due to immunization with DCs treated with BLs, US exposure and OVA. Untreated mice were used as controls to confirm the development of cancer following the first inoculation with E.G7-OVA cells. All treated groups contained five mice.

2.12. Treatment of tumor-bearing mice with antigen-pulsed DCs

E.G7-OVA cells (1×10^6 cells) were intradermally inoculated into the backs of C57BL/6 mice. On day 9, when the tumors were between 8–10 mm, OVA pulsed DCs (1×10^6 cells) prepared as described above were intradermally injected into the backs of the mice. On day 12, DCs were injected similarly. Tumor sizes were monitored from the day of inoculation. All treated groups contained five mice.

2.13. Statistical analysis

Differences in IL-2 secretion between the experimental groups were compared using non-repeated measures ANOVA and Dunnett's test.

3. Results

3.1. Antigen delivery by BLs and sonoporation into the cytosol of DCs lacking the endocytosis pathway

We examined antigen trafficking following delivery using a combination of BLs and US exposure (Fig. 1(a)). In DCs treated with Alexa-OVA in the presence or absence of either BLs or US exposure, the fluorescence from Alexa-OVA appeared as dots in the cytosol. On the other hand, in DCs treated with Alexa-OVA, BLs and US exposure, the fluorescence appeared as dots, but also as diffused fluorescence in the cytosol. To confirm this, antigen delivery was examined following inhibition of the endocytosis pathway in DCs by treatment with sodium azide (Fig. 1(b)). In DCs treated with Alexa-OVA either with or without BLs or US exposure, the fluorescence derived from Alexa-OVA was not observed. On the other hand, in DCs treated with Alexa-OVA, BLs and US exposure, fluorescence was observed in the cytosol even when the endocytosis pathway in DCs was inhibited. In addition, the efficiency of antigen delivery following inhibition of the endocytosis pathway was assessed using flow cytometory (Fig. 1(c)). The fluorescence intensity of DCs treated with Alexa-OVA, BLs and US exposure was higher than that of DCs treated with Alexa-OVA alone, or of Alexa-OVA and BLs or US exposure. These data support the data shown in Fig. 1(b), indicating that Alexa-OVA is observed in the cytosol when DCs are only treated with BLs and US exposure, even when the endocytosis pathway is

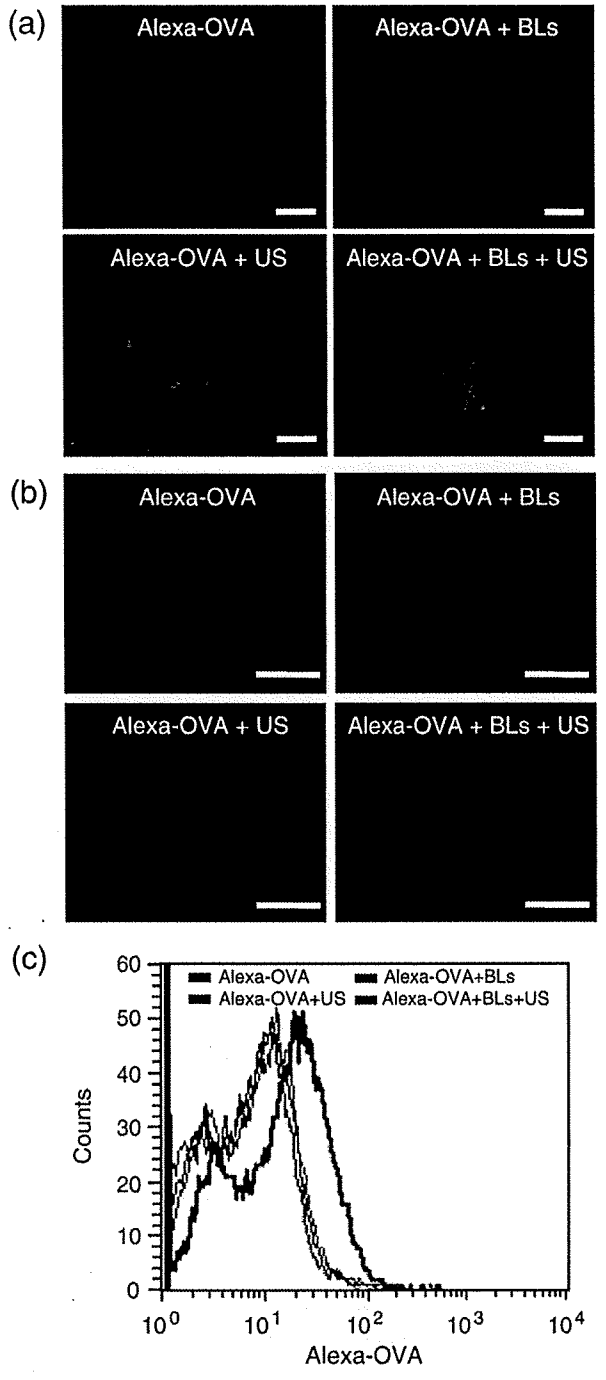

Fig. 1. Intracellular antigen delivery into DCs using BLs and US exposure. (a) Uptake of Alexa-OVA into DCs. DCs were cultured in a glass bottom dish overnight. After washing the cells, Alexa-OVA was added to the dish. Then, the DCs were exposed to US in the presence or absence of BLs and incubated for 1 h at 37 °C. The DCs were washed with PBS, fixed, and the nuclei were stained with propidium iodide. The uptake of Alexa-OVA was observed using a confocal laser microscope. (b) Intracellular delivery of Alexa-OVA into DCs using BLs and US. DCs were pretreated with OptiMEM containing 10 mM NaN_3 for 1 h at 4 °C to inhibit the endocytosis pathway. After washing the cells, Alexa-OVA was added to the DCs in OptiMEM containing10 mM NaN_3. Then, the DCs were exposed to US in the presence or absence of BLs. After US exposure, the DCs were washed with PBS containing 10 mM NaN_3, fixed, and the nuclei were stained with propidium iodide. Intracellular trafficking of Alexa-OVA in the DCs was observed using a confocal laser microscope. Scale bar shows 5 μm. (c) Flow cytometry analysis of DCs containing Alexa-OVA delivered using BLs and US. Alexa-OVA was delivered into the cell interior of the DCs during endocytosis inhibition. After washing the cells, the DCs were analyzed by flow cytometry.

inhibited. These results suggest that the combination of BLs and US exposure can be used to directly deliver antigens into the cytosol of DCs in the absence of endocytosis.

3.2. MHC class I presentation of exogenous antigen delivered into DCs by BLs and US exposure

Exogenous antigen delivered into the cytosol of DCs by BLs and US exposure is recognized as endogenous antigen by DCs and leads to the efficient presentation of peptides derived from exogenous antigens on MHC class I molecules. Thus, we examined whether antigen delivery by BLs and US exposure resulted in the efficient presentation of peptides on MHC class I molecules and the stimulation of $CD8^+$ T cells. C57BL/6-derived OVA-specific T cell hybridoma CD8-OVA1.3 was co-cultured with mouse bone marrow-derived DCs pulsed with antigen. As shown in Fig. 2, CD8-OVA1.3 cells stimulated with DCs pulsed with soluble OVA, either treated or untreated by BLs or US exposure did not secrete a significant amount of IL-2. Of note, a larger amount of IL-2 was secreted by CD8-OVA1.3 cells stimulated with DCs pulsed with OVA treated with a combination of BLs and US exposure. These data indicate that antigen delivery by BLs to DCs upon sonoporation results in the presentation of peptides derived from OVA on MHC class I molecules. In this data, the level of IL-2 secretion increased depending on OVA concentration and reached plateau in 100 μg/ml of OVA concentration. Therefore, we used this OVA concentration (100 μg/ml) in further examinations.

3.3. Cytotoxicity to DCs by the treatment of BLs and US exposure

In this antigen delivery system using BLs and US exposure, the transient pores would be provided on the membrane of DCs. Therefore, it is concerned that the DCs are injured by US exposure in the presence of BLs. To assess the cytotoxicity to DCs by the treatment of BLs and US exposure, we examined about the viability of DCs (Fig. 3). In the treatment of DC with BLs and/or US exposure, the viability of DCs treated with BLs, US exposure or BLs/US exposure was 83 ± 11%, 96 ± 5% or 87 ± 13%, respectively. This result shows that there is not serious damage to DCs even under the condition of inducing transient pores on the membrane of DCs treated with BLs and US exposure.

3.4. Induction of antigen-specific CTL response in the immunization of DCs pulsed with antigen using BLs and US exposure

To examine whether efficient peptide presentation on MHC class I molecules leads to strong induction of antigen-specific CTLs *in vivo*, we immunized C57BL/6 mice twice with bone marrow-derived DCs that had been treated with various antigen delivery techniques. Thereafter, splenocytes were isolated, and a cytotoxicity assay was

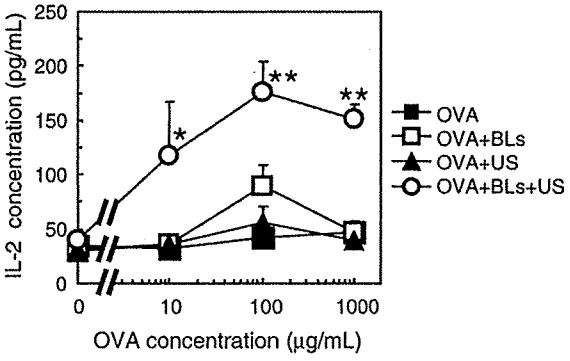

Fig. 2. MHC class I restricted OVA presentation after OVA delivery into DCs using a combination of BLs and US exposure. DCs were pulsed with OVA alone or OVA in conjunction with US exposure and/or BLs. After US exposure, the DCs were incubated for 1 h at 37 °C, then washed with PBS. After culturing for 24 h, the DCs were co-cultured with CD8-OVA1.3 cells for 20 h. The concentration of IL-2 in the supernatants was measured. Each data represents the mean±S.D. for triplicate measurements. *$P<0.05$ compared to the group treated with BLs or US, or without BLs and US. **$P<0.01$ compared to the group treated with BLs or US, or without BLs and US.

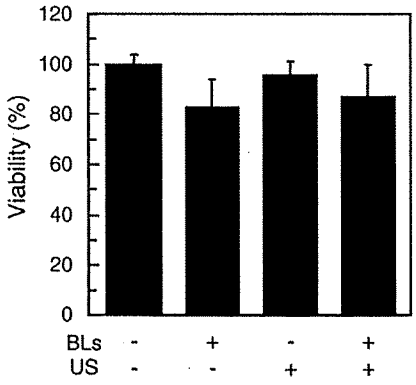

Fig. 3. Viability of DCs treated with BLs and /or US exposure. DCs were treated with BLs and/or US. After US exposure, DCs were incubated for 1 h at 37 °C, then washed with PBS. After culturing for 48 h, the viability of DCs was measured by MTT assay. Each data represents the mean±S.D. for triplicate measurements.

performed using the syngeneic lymphoma cell line EL-4 or its OVA transfectant, E.G7-OVA. As shown in Fig. 4, immunization with DCs without OVA, DCs pulsed with OVA, or OVA combined with BLs or US exposure, induced weak cytotoxicity of splenocytes against the OVA-expressing cell line E.G7-OVA. In contrast, immunization with DCs pulsed with OVA following BL and US exposure resulted in strong cytotoxicity against the OVA-expressing cell line E.G7-OVA by splenocytes. Splenocytes from mice immunized with DCs pulsed using any method of antigen delivery did not exhibit strong cytotoxicity against the parental cell line EL-4. These data indicate that DCs pulsed with antigen using BLs and US exposure as the antigen delivery method efficiently present peptides on MHC class I molecules, which results in strong induction of antigen-specific CTLs *in vivo*.

3.5. Antitumor effects in the immunization of DCs pulsed with antigen by BLs and US exposure

Using an E.G7-OVA tumor model, we examined whether the strong induction of CTLs by antigen delivery with BLs and US exposure leads to efficient anti-tumor immune responses *in vivo*. We immunized C57BL/6 mice twice with bone marrow-derived DCs that had been pulsed using one of two methods of antigen delivery (OVA with US exposure, or OVA with BLs and US exposure). One week after the second immunization, the mice were inoculated intradermally with E.G7-OVA cells, and tumor growth was monitored. As shown in Fig. 5(a) and (b), immunization with untreated DCs weakly suppressed tumor growth. The survival rate of mice immunized with untreated DCs was slightly prolonged, suggesting that non-specific inflammatory responses induced by the injection of DCs result in weak anti-tumor immune responses. Immunization with DCs that had been pulsed with OVA using US exposure suppressed tumor growth slightly more efficiently than the control immunization. Of note, immunization with DCs that had been pulsed with OVA using BLs and US exposure completely suppressed tumor growth, with all mice in this group surviving more than 70 days after tumor inoculation. In addition, we examined the prevention of tumor growth recurrence after re-inoculation of tumor cells into mice, which had completely rejected the first injection of tumor cells (Fig. 5(c)). All mice, which were re-inoculated with E.G7-OVA cells 10 weeks after the first inoculation, completely rejected the tumor cells.

Finally, we examined whether immunization with DCs pulsed with antigen using BLs and US exposure can efficiently suppress the growth of established tumors. For this purpose, we inoculated C57BL/6 mice with E.G7-OVA, and after 9 and 12 days, when the tumors were between 100–200 mm^3, DCs were injected intradermally. As shown in Fig. 6(a), administration of untreated DCs did not provide a significant therapeutic effect. Administration of DCs pulsed with OVA using US exposure exhibited a weak therapeutic effect. Importantly, administration of DCs pulsed with OVA using BLs and US exposure exhibited stronger therapeutic effects in two of the five mice, with these two mice surviving for more than 60 days (Fig. 6(b)). These data indicate that antigen delivery into DCs with BLs and US exposure can induce significant therapeutic effects on established tumors.

4. Discussion

Subunit vaccines utilizing MHC class I-binding peptides have significant limitations that hinder their application to the general patient population (restrictions of HLA types) and that also affect their clinical effectiveness (monovalency of tumor specific antigen) in DC-based tumor immunotherapy. Utilization of tumor associated proteins as antigens may overcome this limitation, thereby enabling a broad spectrum of peptide presentation. In fact, patients treated with tumor cell lysates pulsed DCs showed better response rates compared with patients treated with peptide pulsed DCs [40]. This clinical trial suggests that tumor lysates are a good source of tumor antigens for a polyvalent antitumor vaccine. On the other hand, MHC class I molecules generally present endogenous antigens, whereas exogenous antigens for DCs are taken up by the endocytosis pathway and exogenous antigen-derived peptides are presented on MHC class II molecules [3]. In this study, we showed that by using a combination of BLs and US exposure, exogenous antigen was directly delivered into the cytosol of DCs (Fig. 1) and was presented on MHC class I molecules (Fig. 2). In addition, DCs immunized with antigen delivered by BLs and US exposure could stimulate antigen-specific CTL activation (Fig. 4) and resulted in inducing effective anti-tumor immune responses in tumor-bearing mice. (Figs. 5 and 6) Although peptide and protein delivery with sonoporation using microbubbles have been previously reported [28,29,41], the present study is the first report of effective antigen delivery into DCs by BLs using sonoporation for cancer immunotherapy.

Sonoporation and microbubbles such as Optison have been reported to be an effective gene delivery method using non-viral vectors. In addition, peptide and protein delivery with microbubbles and US exposure has been reported [28,29,41]. In the reports, Bekeredjian et al. showed the feasibility of microbubbles and US exposure for delivery of bioactive protein (luciferase, 60 kDa) into the cytosol of *in vitro* and *in vivo* cells [28,29]. Larina I.V. et al. reported that FITC-dextrans of 10–2000 kDa were delivered into human breast

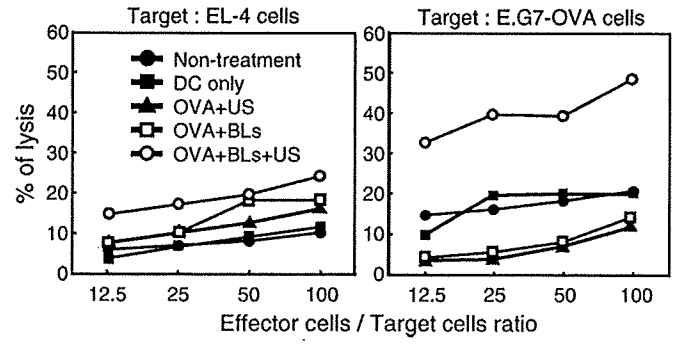

Fig. 4. Antigen specific CTL induction after immunization with DCs treated with BLs and US exposure. DCs were pulsed with OVA under each condition and cultured. After washing the cells, the DCs were intradermally injected into the backs of C57BL/6 mice. After 7 days, the mice were re-immunized. Seven days after the second immunization, splenocytes were obtained and stimulated with mitomycin C-treated E.G7-OVA cells at a ratio of 10:1 for 5 days. The stimulated splenocytes were used as effector cells for a cytotoxicity assay, using EL-4 or E.G7-OVA cells as the target in a flow cytometric assay.

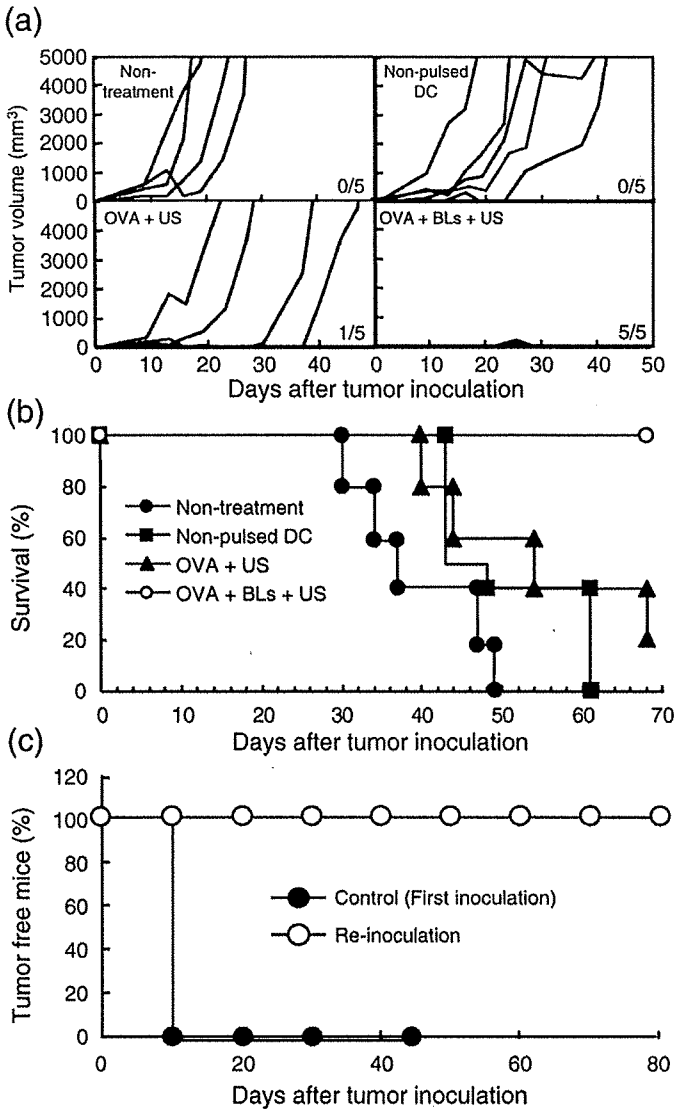

Fig. 5. Antitumor effect caused by immunization of DCs treated with antigen, BLs and US exposure. C57BL/6 mice were immunized with DCs twice. Seven days after the second immunization, E.G7-OVA cells were intradermally inoculated into the backs of the mice, and the tumor volume and survival of the mice was monitored. (a): Tumor volume of the mice after tumor inoculation. Each line indicates the tumor volume in an individual mouse. The fractional number in the lower right of each group shows the number of mice completely rejecting tumors / the number of total experimental mice. (b): Survival rate of the mice after tumor inoculation. (c): Tumor rejection efficiency after re-inoculation with tumor cells. E.G7-OVA cells were re-injected into the mice, which had rejected tumor cells following immunization with DCs treated with OVA, BLs and US in a prior immunization (a). Normal mice were used as controls to confirm the development of cancer following the first inoculation with E.G7-OVA cells. All treated groups contained five mice.

adenocarcinoma (MCF7) by the combination of Optison (conventional microbubbles) and US exposure [42]. It is believed that the delivery mechanism is due to the presence of transient pores through the cell membrane, resulting in extracellular molecules being directly delivered into the cytosol [22,43]. As shown in Fig. 1(b), antigen was directly delivered into DCs by the combination of BLs and US exposure even when the endocytosis pathway was inhibited. Therefore, it is thought that the antigen delivery mechanism induced by BLs and sonoporation is the same as that induced by microbubbles and sonoporation. In studies using microbubbles and sonoporation, pore sizes (based on the physical diameter of the component compounds) were typically between 30–100 nm, and estimates of the membrane recovery time ranged from a few seconds to a few minutes [44]. On the other hand, in studies on the aftereffects of US exposure on cell membranes, Eshet *et al.* reported that microbubbles resulted in a rougher cell surface characterized by depressions, but that the effects are reversible within 24 h following US exposure [43]. In the present study, DCs were incubated with antigen for 1 h after US exposure and increased the delivery efficiency of antigen into the cytosol of DCs. We confirmed the efficiency of MHC class I antigen presentation in DCs with/without 1 h incubation after US exposure. The efficiency following 1 h incubation was higher than that without incubation (data not shown). This result suggests that the membrane permeability of DCs increases even after US exposure. Although the mechanism behind antigen delivery by BLs is unknown, our data support a temporary increase in permeability of the plasma membrane after US exposure. Moreover, recent data from microbubble studies suggest that the resealing of US-induced pores is an energy-dependent process, with the cells exhibiting morphological features consistent with an active and vesicle-based wound-healing responses [45]. Therefore, cells treated with sonoporation are viable due to this recovery mechanism. In this study, the viability of the DCs treated with BLs and US exposure was maintained more than 85% (Fig. 3). The accumulated evidence suggests that the combination of BLs and US exposure is an unique antigen delivery system which can deliver exogenous antigens into the cytosol without serious damage to DCs.

In this study, exogenous antigens, directly delivered into the cytosol of DCs by means of BLs and US exposure, were presented on MHC class I molecules. In addition, immunization of DCs treated with antigen, BLs and US exposure effectively primed antigen-specific CTLs. On the other hand, MHC class I antigen presentation lead to low-level

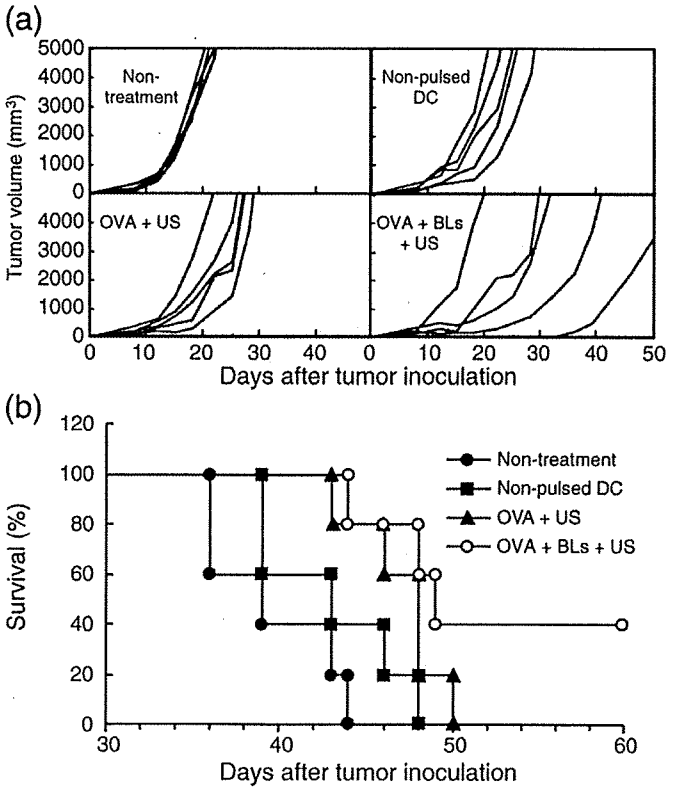

Fig. 6. Immunization of DCs treated with antigen, BLs and US exposure: therapeutic effect on tumor growth. E.G7-OVA cells were intradermally inoculated into the backs of C57BL/6 mice. On day 9, at a tumor size of 8–10 mm, OVA pulsed DCs were intradermally injected into the backs of the mice. On day 12, DCs were injected similarly. The tumor volume and survival of the mice was monitored. (a): Tumor volume of the mice after tumor inoculation. Each line indicates the tumor volume in individual mice. (b): Survival rate of the mice after tumor inoculation. All treated groups contained five mice.

antigen delivery with either BLs or US exposure. In these treated cells, antigen was mainly taken up via the endocytosis pathway. Although we have not confirmed MHC class II presentation, the antigen would presumably be presented on MHC class II molecules to DCs via the general antigen processing mechanism [10]. The exogenous antigens directly delivered into the cytosol would be processed similarly endogenously derived antigens, which are enzymatically digested into peptides, mainly by cytosolic proteases called proteasomes, and are then transported by transporters associated with antigen processing (TAP) molecules into the endoplasmic reticulum (ER). In the ER lumen, peptides bind to MHC class I molecules, which are subsequently transported via the Golgi apparatus to the cell surface [46]. Moreover, immunization of DCs treated with OVA, BLs and US exposure could prime OVA-specific CTLs. This result indicates that DCs presented with OVA-derived epitope peptides on MHC class I molecules effectively prime OVA-specific CTLs *in vivo*. We suspected that the effective priming of antigen-specific CTLs would result in the rejection of tumor cells. As shown in Fig. 5(a), all the immunized mice completely rejected the inoculated tumor cells. Tumor cells were intradermally re-injected into these mice to re-challenge their immune system and assess the preventive effects of immunization for suppressing tumor regeneration (Fig. 5(c)). Rejection following re-challenge with tumor cells suggests the induction of an antigen memory system in the host's immune system, i.e., memory T cells for the immunization antigen. Thus, this therapeutic method has potential for suppressing the regeneration and metastasis of tumors. Finally, we also assessed the therapeutic effects of this treatment towards established tumors (Fig. 6). Immunization with DCs treated with antigen, BLs and US exposure lead to significant therapeutic effects towards established tumors. Tumor cells generally secrete cytokines such as TGF-β to suppress the host's immune system. It is therefore possible that antigen delivery with BLs and US exposure could effectively induce an anti-tumor immune response even in the presence of established tumors.

In conclusion, we have developed a novel system for delivering antigens into DCs using BLs and sonoporation. Immunization of DCs using this antigen delivery system could effectively prime the anti-tumor immune system due to the induction of MHC class I TAA presentation. Therefore, BLs in conjunction with sonoporation might be a useful antigen delivery system for DC-based cancer immunotherapy. In the future, this system will be applied to various antigens containing unknown TAAs, such as crude antigens separated from surgically-removed human tumors.

Acknowledgments

The authors thank Mr. Shota Otake, Mr. Norihito Nishiie, Mr. Ken Osawa, Ms. Risa Koshima, Ms. Motoka Kawamura, Mr. Ryo Tanakadate, Mr. Kunihiko Matsuo and Mr. Yasuyuki Shiono (Teikyo University) for their technical assistance, and Mr. Yasuhiko Hayakawa, Mr. Takahiro Yamauchi and Mr. Kosho Suzuki (Nepa Gene Co., Ltd.) for their technical advice regarding US exposure. This study was supported by the Program for Promotion of Fundamental Studies in Health Sciences of the National Institute of Biomedical Innovation (NIBIO). Tetsuya Kodama acknowledges the Grant for Research on Nanotechnical Medical, the Ministry of Health, Labour and Welfare of Japan (H19-nano-010).

References

[1] F.O. Nestle, A. Farkas, C. Conrad, Dendritic-cell-based therapeutic vaccination against cancer, Curr. Opin. Immunol. 17 (2005) 163–169.
[2] J. Copier, A. Dalgleish, Overview of tumor cell-based vaccines, Int. Rev. Immunol. 25 (2006) 297–319.
[3] R.N. Germain, MHC-dependent antigen processing and peptide presentation: providing ligands for T lymphocyte activation, Cell 76 (1994) 287–299.
[4] P. Elamanchili, M. Diwan, M. Cao, J. Samuel, Characterization of poly(D,L-lactic-co-glycolic acid) based nanoparticulate system for enhanced delivery of antigens to dendritic cells, Vaccine 22 (2004) 2406–2412.
[5] T. Yoshikawa, N. Okada, A. Oda, K. Matsuo, K. Matsuo, Y. Mukai, Y. Yoshioka, T. Akagi, M. Akashi, S. Nakagawa, Development of amphiphilic gamma-PGA-nanoparticle based tumor vaccine: potential of the nanoparticulate cytosolic protein delivery carrier, Biochem. Biophys. Res. Commun. 366 (2008) 408–413.
[6] P. Machy, K. Serre, L. Leserman, Class I-restricted presentation of exogenous antigen acquired by Fcgamma receptor-mediated endocytosis is regulated in dendritic cells, Eur. J. Immunol. 30 (2000) 848–857.
[7] N. Okada, T. Saito, K. Mori, Y. Masunaga, Y. Fujii, J. Fujita, K. Fujimoto, T. Nakanishi, K. Tanaka, S. Nakagawa, T. Mayumi, T. Fujita, A. Yamamoto, Effects of lipofectin-antigen complexes on major histocompatibility complex class I-restricted antigen presentation pathway in murine dendritic cells and on dendritic cell maturation, Biochim. Biophys. Acta 1527 (2001) 97–101.
[8] L. Wang, H. Ikeda, Y. Ikuta, M. Schmitt, Y. Miyahara, Y. Takahashi, X. Gu, Y. Nagata, Y. Sasaki, K. Akiyoshi, J. Sunamoto, H. Nakamura, K. Kuribayashi, H. Shiku, Bone marrow-derived dendritic cells incorporate and process hydrophobized polysaccharide/oncoprotein complex as antigen presenting cells, Int. J. Oncol. 14 (1999) 695–701.
[9] K. Kawamura, N. Kadowaki, R. Suzuki, S. Udagawa, S. Kasaoka, N. Utoguchi, T. Kitawaki, N. Sugimoto, N. Okada, K. Maruyama, T. Uchiyama, Dendritic cells that endocytosed antigen-containing IgG-liposomes elicit effective antitumor immunity, J. Immunother. 29 (2006) 165–174.
[10] K.W. Kim, S.H. Kim, J.H. Jang, E.Y. Lee, S.W. Park, J.H. Um, Y.J. Lee, C.H. Lee, S. Yoon, S.Y. Seo, M.H. Jeong, S.T. Lee, B.S. Chung, C.D. Kang, Dendritic cells loaded with exogenous antigen by electroporation can enhance MHC class I-mediated antitumor immunity, Cancer Immunol. Immunother. 53 (2004) 315–322.
[11] J.M. Weiss, C. Allen, R. Shivakumar, S. Feller, L.H. Li, L.N. Liu, Efficient responses in a murine renal tumor model by electroloading dendritic cells with whole-tumor lysate, J. Immunother. 28 (2005) 542–550.
[12] M. Fechheimer, J.F. Boylan, S. Parker, J.E. Sisken, G.L. Patel, S.G. Zimmer, Transfection of mammalian cells with plasmid DNA by scrape loading and sonication loading, Proc. Natl. Acad. Sci. U. S. A. 84 (1987) 8463–8467.
[13] M.W. Miller, D.L. Miller, A.A. Brayman, A review of in vitro bioeffects of inertial ultrasonic cavitation from a mechanistic perspective, Ultrasound Med. Biol. 22 (1996) 1131–1154.
[14] M. Joersbo, J. Brunstedt, Protein synthesis stimulated in sonicated sugar beet cells and protoplasts, Ultrasound Med. Biol. 16 (1990) 719–724.
[15] D.L. Miller, S.V. Pislaru, J.E. Greenleaf, Sonoporation: mechanical DNA delivery by ultrasonic cavitation, Somat. Cell Mol. Genet. 27 (2002) 115–134.
[16] H.R. Guzman, A.J. McNamara, D.X. Nguyen, M.R. Prausnitz, Bioeffects caused by changes in acoustic cavitation bubble density and cell concentration: a unified explanation based on cell-to-bubble ratio and blast radius, Ultrasound Med. Biol. 29 (2003) 1211–1222.
[17] W. Wei, B. Zheng-zhong, W. Yong-jie, Z. Qing-wu, M. Ya-lin, Bioeffects of low-frequency ultrasonic gene delivery and safety on cell membrane permeability control, J. Ultrasound Med. 23 (2004) 1569–1582.
[18] H.J. Kim, J.F. Greenleaf, R.R. Kinnick, J.T. Bronk, M.E. Bolander, Ultrasound-mediated transfection of mammalian cells, Hum. Gene Ther. 7 (1996) 1339–1346.
[19] D.B. Tata, F. Dunn, D.J. Tindall, Selective clinical ultrasound signals mediate differential gene transfer and expression in two human prostate cancer cell lines: LnCap and PC-3, Biochem. Biophys. Res. Commun. 234 (1997) 64–67.
[20] M. Duvshani-Eshet, M. Machluf, Therapeutic ultrasound optimization for gene delivery: a key factor achieving nuclear DNA localization, J. Control. Release 108 (2005) 513–528.
[21] W.J. Greenleaf, M.E. Bolander, G. Sarkar, M.B. Goldring, J.F. Greenleaf, Artificial cavitation nuclei significantly enhance acoustically induced cell transfection, Ultrasound Med. Biol. 24 (1998) 587–595.
[22] Y. Taniyama, K. Tachibana, K. Hiraoka, M. Aoki, S. Yamamoto, K. Matsumoto, T. Nakamura, T. Ogihara, Y. Kaneda, R. Morishita, Development of safe and efficient novel nonviral gene transfer using ultrasound: enhancement of transfection efficiency of naked plasmid DNA in skeletal muscle, Gene Ther. 9 (2002) 372–380.
[23] S. Chen, J.H. Ding, R. Bekeredjian, B.Z. Yang, R.V. Shohet, S.A. Johnston, H.E. Hohmeier, C.B. Newgard, P.A. Grayburn, Efficient gene delivery to pancreatic islets with ultrasonic microbubble destruction technology, Proc. Natl. Acad. Sci. U. S. A. 103 (2006) 8469–8474.
[24] A. Aoi, Y. Watanabe, S. Mori, M. Takahashi, G. Vassaux, T. Kodama, Herpes simplex virus thymidine kinase-mediated suicide gene therapy using nano/microbubbles and ultrasound, Ultrasound Med. Biol. 34 (2008) 425–434.
[25] Z.P. Shen, A.A. Brayman, L. Chen, C.H. Miao, Ultrasound with microbubbles enhances gene expression of plasmid DNA in the liver via intraportal delivery, Gene Ther. (2008).
[26] S. Sonoda, K. Tachibana, E. Uchino, A. Okubo, M. Yamamoto, K. Sakoda, T. Hisatomi, K.H. Sonoda, Y. Negishi, Y. Izumi, S. Takao, T. Sakamoto, Gene transfer to corneal epithelium and keratocytes mediated by ultrasound with microbubbles, Investig. Ophthalmol. Vis. Sci. 47 (2006) 558–564.
[27] K. Iwanaga, K. Tominaga, K. Yamamoto, M. Habu, H. Maeda, S. Akifusa, T. Tsujisawa, T. Okinaga, J. Fukuda, T. Nishihara, Local delivery system of cytotoxic agents to tumors by focused sonoporation, Cancer Gene Ther. 14 (2007) 354–363.
[28] R. Bekeredjian, S. Chen, P.A. Grayburn, R.V. Shohet, Augmentation of cardiac protein delivery using ultrasound targeted microbubble destruction, Ultrasound Med. Biol. 31 (2005) 687–691.
[29] R. Bekeredjian, H.F. Kuecherer, R.D. Kroll, H.A. Katus, S.E. Hardt, Ultrasound-targeted microbubble destruction augments protein delivery into testes, Urology 69 (2007) 386–389.
[30] T. Yamashita, S. Sonoda, R. Suzuki, N. Arimura, K. Tachibana, K. Maruyama, T. Sakamoto, A novel bubble liposome and ultrasound-mediated gene transfer to ocular surface: RC-1 cells in vitro and conjunctiva in vivo, Exp. Eye Res. 85 (2007) 741–748.

[31] R. Suzuki, T. Takizawa, Y. Negishi, K. Hagisawa, K. Tanaka, K. Sawamura, N. Utoguchi, T. Nishioka, K. Maruyama, Gene delivery by combination of novel liposomal bubbles with perfluoropropane and ultrasound, J. Control. Release 117 (2007) 130–136.
[32] R. Suzuki, T. Takizawa, Y. Negishi, N. Utoguchi, K. Maruyama, Effective gene delivery with novel liposomal bubbles and ultrasonic destruction technology, Int. J. Pharm. 354 (2008) 49–55.
[33] R. Suzuki, T. Takizawa, Y. Negishi, N. Utoguchi, K. Sawamura, K. Tanaka, E. Namai, Y. Oda, Y. Matsumura, K. Maruyama, Tumor specific ultrasound enhanced gene transfer in vivo with novel liposomal bubbles, J. Control. Release 125 (2008) 137–144.
[34] R. Suzuki, T. Takizawa, Y. Negishi, N. Utoguchi, K. Maruyama, Effective gene delivery with liposomal bubbles and ultrasound as novel non-viral system, J. Drug Target. 15 (2007) 531–537.
[35] J.D. Pfeifer, M.J. Wick, R.L. Roberts, K. Findlay, S.J. Normark, C.V. Harding, Phagocytic processing of bacterial antigens for class I MHC presentation to T cells, Nature 361 (1993) 359–362.
[36] K. Inaba, M. Inaba, M. Deguchi, K. Hagi, R. Yasumizu, S. Ikehara, S. Muramatsu, R.M. Steinman, Granulocytes, macrophages, and dendritic cells arise from a common major histocompatibility complex class II-negative progenitor in mouse bone marrow, Proc. Natl. Acad. Sci. U. S. A. 90 (1993) 3038–3042.
[37] D.P. Guo, X.Y. Li, P. Sun, Y.B. Tang, X.Y. Chen, Q. Chen, L.M. Fan, B. Zang, L.Z. Shao, X.R. Li, Ultrasound-targeted microbubble destruction improves the low density lipoprotein receptor gene expression in HepG2 cells, Biochem. Biophys. Res. Commun. 343 (2006) 470–474.
[38] T. Mosmann, Rapid colorimetric assay for cellular growth and survival: application to proliferation and cytotoxicity assays, J. Immunol. Methods 65 (1983) 55–63.
[39] S.E. Slezak, P.K. Horan, Cell-mediated cytotoxicity. A highly sensitive and informative flow cytometric assay, J. Immunol. Methods 117 (1989) 205–214.
[40] G. Reinhard, A. Marten, S.M. Kiske, F. Feil, T. Bieber, I.G. Schmidt-Wolf, Generation of dendritic cell-based vaccines for cancer therapy, Br. J. Cancer 86 (2002) 1529–1533.
[41] M. Kinoshita, K. Hynynen, Intracellular delivery of Bak BH3 peptide by microbubble-enhanced ultrasound, Pharm. Res. 22 (2005) 716–720.
[42] I.V. Larina, B.M. Evers, R.O. Esenaliev, Optimal drug and gene delivery in cancer cells by ultrasound-induced cavitation, Anticancer Res. 25 (2005) 149–156.
[43] M. Duvshani-Eshet, D. Adam, M. Machluf, The effects of albumin-coated microbubbles in DNA delivery mediated by therapeutic ultrasound, J. Control. Release 112 (2006) 156–166.
[44] C.M. Newman, T. Bettinger, Gene therapy progress and prospects: ultrasound for gene transfer, Gene Ther. 14 (2007) 465–475.
[45] R.K. Schlicher, H. Radhakrishna, T.P. Tolentino, R.P. Apkarian, V. Zarnitsyn, M.R. Prausnitz, Mechanism of intracellular delivery by acoustic cavitation, Ultrasound Med. Biol. 32 (2006) 915–924.
[46] P.M. Kloetzel, Antigen processing by the proteasome, Nat. Rev. Mol. Cell. Biol. 2 (2001) 179–187.

Journal of Controlled Release 140 (2009) 306–311

Contents lists available at ScienceDirect

Journal of Controlled Release

journal homepage: www.elsevier.com/locate/jconrel

Enhanced magnetic resonance imaging of experimental pancreatic tumor *in vivo* by block copolymer-coated magnetite nanoparticles with TGF-β inhibitor

Michiaki Kumagai [a,e,1], Mitsunobu R. Kano [b,f,1], Yasuyuki Morishita [b], Motomi Ota [a], Yutaka Imai [a], Nobuhiro Nishiyama [a,e,f], Masaki Sekino [c], Shoogo Ueno [d], Kohei Miyazono [b,f], Kazunori Kataoka [a,e,f,*]

[a] Department of Materials Engineering, Graduate School of Engineering, The University of Tokyo, 7-3-1 Hongo, Bunkyo-ku, Tokyo 113-8656, Japan
[b] Department of Molecular Pathology, Graduate School of Medicine, The University of Tokyo, 7-3-1 Hongo, Bunkyo-ku Tokyo 113-0033, Japan
[c] Department of Advanced Energy, Graduate School of Frontier Sciences, The University of Tokyo, 5-1-5, Kashiwanoha, Kashiwa-shi, Chiba, 277-8561, Japan
[d] Department of Applied Quantum Physics, Graduate School of Engineering, Kyushu University, 6-10-1 Hakozaki, Higashi-ku Fukuoka 812-8581, Japan
[e] Center for Disease Biology and Integrative Medicine, School of Medicine, The University of Tokyo, 7-3-1 Hongo, Bunkyo-ku, Tokyo 113-0033, Japan
[f] Center for NanoBio Integration, The University of Tokyo, 7-3-1 Hongo, Bunkyo-ku, Tokyo 113-8656, Japan

ARTICLE INFO

Article history:
Received 13 March 2009
Accepted 5 June 2009
Available online 12 June 2009

Keyword:
Magnetic resonance imaging
Pancreatic cancer
TGF-β
Magnetite nanoparticles
Poly(ethylene glycol)

ABSTRACT

Early detection of solid tumors, particularly pancreatic cancer, is of substantial importance in clinics. Enhanced magnetic resonance imaging (MRI) with iron oxide nanoparticles is an available way to detect the cancer. The effective and selective accumulation of these nanoparticles in the tumor tissue is needed for improved imaging, and in this regard, their longevity in the blood circulation time is crucial. We developed here block copolymer-coated magnetite nanoparticles for pancreatic cancer imaging, by means of a chelation between the carboxylic acid groups in poly(ethylene glycol)–poly(aspartic acid) block copolymer (PEG–PAsp) and Fe on the surface of the iron oxide nanoparticles. These nanoparticles had considerably narrow distribution, even upon increased ionic strength or in the presence of fetal bovine serum. The PEG–PAsp-coated nanoparticles were further shown to be potent as a contrast agent for enhanced MRI for an experimental pancreatic cancer, xenografts of the human-derived BxPC3 cell line in BALB/c nude mice, with combined administration of TGF-β inhibitor. Iron staining of tumor tissue confirmed the accumulation of the nanoparticles in tumor tissue. Use of the PEG–PAsp-coated magnetite nanoparticles, combined with the TGF-β inhibitor, is of promising clinical importance for the detection of intractable solid cancers, including pancreatic cancer.

1. Introduction

Pancreatic cancer, one of the intractable solid tumors, is the fourth leading cause of cancer-related deaths in the United States and the fifth in Japan [1]. The average survival period of patients suffering from advanced pancreatic adenocarcinoma is still extremely short, only 6 months, despite recent progress in the chemotherapies [2]. Although cancer detection and treatment have been greatly improved through the development of diagnostic imaging modalities, it is still difficult to detect pancreatic cancer [3]. Consequently, the development of diagnostic systems to detect these cancers is of great importance.

Recently, superparamagnetic iron oxide (SPIO) nanoparticles composed of either magnetite (Fe_3O_4) or maghemite (g-Fe_2O_3) have been studied as contrast agents for magnetic resonance (MR) imaging [4]. Commercial application for human diagnosis based on SPIO particles is currently available. However, since cancer detection requires the systemic administration of iron oxide nanoparticles, the circulation time of the particles must be prolonged. Several studies have already reported that the behavior of magnetic nanoparticles in the bloodstream depends closely on their nanoscale morphology, including overall diameter, size distribution, or nature of the surface [5,6]. Additionally, the surface modification of iron oxide nanoparticles has proved a versatile strategy for improving their biological performance, including the reduction of immunogenicity and enhancement of targeted delivery to specific tissues [7]. However, the overall correlation between the surface modification of nanoparticles and their *in vivo* behavior remains to be further elucidated.

Various methods of stabilization for SPIO nanoparticles have been reported to date [8]. One of the most feasible approaches could be the stabilization of SPIO by coated with biocompatible polymers [9]. Suitable polymers, including poly(ethylene glycol) (PEG) and its block copolymers, are promising for the development of SPIO systems with defined surface properties. This coating of particles with PEG, or PEGylation, to avoid their uptake by the reticuloendothelial system, is under intensive investigation. We also previously reported the accumulation of β-FeOOH nanoparticles coated with PEG–poly(α,β-aspartic acid) block copolymer

* Corresponding author. Department of Materials Engineering, Graduate School of Engineering, The University of Tokyo, 7-3-1 Hongo, Bunkyo-ku, Tokyo 113-8656, Japan.
E-mail address: kataoka@bmw.t.u-tokyo.ac.jp (K. Kataoka).
[1] Equal contribution.

0168-3659/$ – see front matter © 2009 Elsevier B.V. All rights reserved.
doi:10.1016/j.jconrel.2009.06.002

(PEG–PAsp) into experimental colon adenocarcinoma, which could be applicable for tumor-selective MR imaging [10]. The multivalent bonding of PEG-based block copolymer to magnetic nanoparticles may thus help to facilitate the accumulation of these nanoparticles into some solid tumors. However, magnetic nanoparticles of any design have not yet been successful in exhibiting sufficient accumulation in intractable solid cancers, including pancreatic adenocarcinoma [1]. In addition to improving the performance of iron-based contrast agents (e.g. biocompatibility), the co-administration of adjuvant small molecules could increase the accumulation of these agents in target cancer tissue. In fact, we have recently shown that the administration of the small molecule TGF-β inhibitor (LY364947) at a low dose [11], which could minimize the potential side effects of the TGF-β inhibitor, can alter the tumor microenvironment and enhance the EPR effect in these cancers [12]. Therefore, the combined use of TGF-β inhibitor could be promising to diagnose intractable cancers with a long-circulating MRI contrast agent. Here, we demonstrated the successful MR imaging of experimental pancreatic cancer by the systemic administration of newly developed SPIO nanoparticles coated by PEG–PAsp in aid of TGF-β inhibitor.

2. Materials and methods

2.1. Reagents

β-benzyl L-aspartate and bis(trichloromethyl)carbonate (triphosgene) were purchased from Sigma-Aldrich Corporation (St. Louis, MO, USA) and Tokyo Chemical Industry Co., Ltd. (Tokyo, Japan), respectively. α-Methoxy-ω-amino-poly(ethylene glycol) (CH_3O–PEG–NH_2; $M_w = 12000$) was purchased from NOF Corporation (Tokyo, Japan). Tetrahydrofuran (THF), *n*-hexane, *N,N*-dimethylformamide (DMF), CH_2Cl_2 were doubly-distilled according to the standard procedures. The magnetite nanoparticles were supplied by Toda Kogyo Corporation (Hiroshima, Japan; average particle size of magnetite: 10 nm). Resovist® was obtained from Bayer HealthCare Co., Ltd. (Osaka, Japan). TGF-β inhibitor was purchased from EMD Chemicals Inc. (San Diego, CA, USA) (LY364947; catalog no. 616451).

2.2. Synthesis of poly(ethylene glycol)–poly(α,β-aspartic acid) block copolymer (PEG–PAsp)

PEG–PAsp was synthesized by a previously reported procedure [13]. Briefly, poly (ethylene glycol)–*b*–poly(β-benzyl L-aspartate) block copolymer (PEG–PBLA) was prepared by ring-opening polymerization of N-carboxy anhydride of β-benzyl L-aspartate (BLA-NCA) from the ω-NH_2 group of PEG ($M_w = 1.2 \times 10^4$). Molecular weight distribution of PEG–PBLA was narrow as $M_w/M_n = 1.06$, which was determined by gel permeation chromatography [columns: TSK-gel G3000HHR, G4000HHR (Tosoh, Yamaguchi, Japan); eluent: DMF containing 10 mM LiCl; flow rate: 0.8 ml/min; detector: refractive index (RI); temperature: 40 °C]. The composition of these block copolymers was determined by ^{1}H NMR from peak intensity ratios of methylene protons of PEG (OCH_2CH_2: $d = 3.7$ ppm) and phenyl protons of the β-benzyl groups of PBLA ($-CH_2C_6H_5$: $d = 7.3$ ppm). The polymerization degree of BLA in block copolymer was calculated to be 38. The benzyl groups of PEG–PBLA were then removed by alkaline hydrolysis using 0.1 N NaOH to obtain PEG–PAsp as follows:

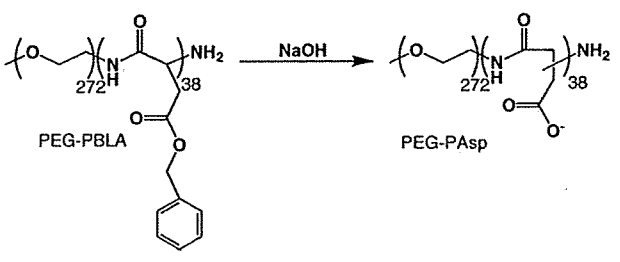

2.3. Preparation of PEG–PAsp-coated magnetite nanoparticles

PEG–PAsp-coated magnetite nanoparticles were prepared according to the previous method with slight modification [10]. Briefly, magnetite solution was quickly added to an aqueous solution of PEG–PAsp with varying feed molar ratios of aspartic acid residues to Fe ([Asp]/[Fe]) in the range of 0.01 to 1. The final concentration of magnetite was adjusted to 10 mmol/l. The mixed solutions were incubated at room temperature for 24 h to obtain magnetite nanoparticles coated with PEG–PAsp. Purification of the PEG–PAsp-coated magnetite nanoparticles was carried out by ultrafiltration (MWCO 200 000; polysulfone membrane, Toyo Roshi Co. Ltd., Tokyo, Japan).

2.4. Physicochemical characterization of the nanoparticles

The morphology and size distribution of the nanoparticles were examined by transmission electron microscopy (H-7000, Hitachi, Ltd., Tokyo, Japan) at an accelerating voltage of 75 kV. The TEM samples were prepared by mounting a drop of aqueous iron oxide nanoparticles suspension on carbon-coated 400 mesh Cu grids and allowing them to dry in air. Fourier transform infrared (FT-IR) spectra were obtained using a FT-IR spectrophotometer (FT/IR615, JASCO Corporation, Hachioji, Tokyo, Japan) with a resolution of 4 cm^{-1}. To characterize the interaction between block copolymer and magnetite nanoparticles, a small amount of nanoparticles powder was milled with KBr, and then pressed into a disc for analysis. Each spectrum was scanned 64 times to increase the signal-to-noise ratio. The Fe content in the nanoparticles was determined by ion coupled plasma-mass spectroscopy (ICP-MS, 4500, Hewlett Packard, Palo Alto, CA, USA). The amount of adsorbed block copolymer on magnetite nanoparticles was measured by thermogravimetric analysis (TGA) (EXSTAR6200 TG/DTA, Seiko Instruments Inc., Chiba, Japan) in nitrogen atmosphere with a heating rate of 10 °C/min in the temperature range of 25–1100 °C.

2.5. Light scattering and ζ-potential measurements

The size distribution of the PEG–PAsp-coated magnetite nanoparticles was examined by dynamic light scattering (DLS) DLS-7000 (Otsuka Electronics Co., Ltd., Osaka, Japan). Vertically polarized light with a wavelength of 488 nm from an Ar-ion laser (15 mW) was used as the incident beam. All measurements were conducted at 37 °C, and the data were analyzed by the cumulant method to determine the hydrodynamic diameters of the particles. The ζ-potential of PEG–PAsp-coated magnetite nanoparticles at 37 °C was measured by a Zetasizer NanoZS instrument equipped with a DTS5001 cell (Malvern Instruments Ltd., Worcestershire, UK).

2.6. Characterization of the r_2 relaxivities

The MR contrast effect of the magnetite nanoparticles was examined by measuring their proton relaxivities, r_2, of which the definition is the slope of the concentration dependence given as:

$$1/T_2 = 1/T_2(0) + r_2[\mathrm{Fe}]$$

Thus, a plot of $1/T_2$ versus concentration gives the relaxivity as the slope, where T_2 is the transversal relaxation time, $1/T_2$ is the transversal relaxation rate constant in the presence of a paramagnetic species, and $1/T_2(0)$ is the transversal relaxation rate constant in the absence of a paramagnetic species. The magnetite nanoparticles were dispersed into deionized water at concentrations of 0.5, 1.0, 1.5, 2.0, and 2.5 mM and the T_2 of these nanoparticle solutions was measured at 25 °C in water with a 0.47 T minispectrometer (Minispec, Bruker

Optics Inc., Woodlands, TX, USA) using the Carr–Purcell–Meiboom–Gill (CPMG) method [14].

2.7. In vivo MR imaging

The BxPC3 human pancreatic adenocarcinoma cell line was obtained from the American Type Culture Collection (Manassas, VA, USA). The BxPC3 cells were grown in RPMI 1640 medium supplemented with 10% FBS. BALB/c nude mice (female, 5–6 weeks of age), obtained from Charles River Laboratories Japan Inc. (Tokyo, Japan), were inoculated subcutaneously with BxPC3 cells (1×10^7 cells/mouse). After 3–4 weeks, MR imaging of the tumors was conducted with a 4.7 T scanner (INOVA200, Varian, Inc., Palo Alto, CA, USA). Twenty-four hours prior to the *in vivo* MR imaging, animals were treated with TGF-β inhibitor, 5 mg/ml in 4 μl of DMSO and diluted by 100 μl of PBS, at 1 mg/kg by intraperitoneal injection. Subsequently, the mice were injected at a dose of 0.1 mmolFe/kg, with Resovist® or PEG–PAsp-coated magnetite nanoparticles. A total of 4 conditions ($n=5$ mice each) were investigated, i.e. with or without TGF-β inhibitor for both Resovist® or PEG–PAsp-coated magnetite nanoparticles. Imaging was performed at different temporal points (e.g., preinjection, 1 h postinjection, and 2 h postinjection). For the T_2-weighted MR imaging of live mice, the following parameters were adopted: spin-echo method, point resolution = 234 × 234 μm, section thickness = 2.0 mm, TE = 60 ms, TR = 3000 ms, number of acquisitions = 5. All animals were treated in accordance with the guidelines of the Animal Ethics Committee of the University of Tokyo.

2.8. Histology

The excised samples were fixed overnight in 4% paraformaldehyde and then paraffin-embedded. Embedded samples were thin sliced at 10 μm thick and then stained using an Iron Stain Kit (Muto Pure Chemicals Co., Ltd., Tokyo, Japan), based on McFadzean's protocol [15], with nuclear post-staining by 1% Safranin O. Iron staining was observed using an AX80 microscope (Olympus Corporation, Tokyo, Japan). The photographs were further quantified using Adobe Photoshop software (Adobe Systems Incorporated, San Jose, CA, USA), ImageJ software (National Institute of Health, MD, USA), and Microsoft Excel software (Microsoft Corporation, Redmond, WA, USA).

3. Results and discussion

3.1. The physicochemical properties of the PEG–PAsp-coated magnetite nanoparticle: diameter and surface polymer density

For solid tumor diagnosis, it is important to develop well-designed magnetite nanoparticles. The key physicochemical properties of magnetite nanoparticles are size, surface polymer density, and surface charge, since these characteristics can affect accumulation of magnetite nanoparticles to solid tumor. The PEG–PAsp-coated magnetite nanoparticles were prepared by mixing solutions of magnetite nanoparticles and PEG–PAsp with various molar ratios of the Asp residues to Fe (Asp/Fe); Asp/Fe ranged from 0.01 to 0.5, where [Fe] = 10 mmol/l. As seen in Fig. 1, the transmission electron microscopy (TEM) image with 75 kV accelerating voltage of nanoparticles mounted on carbon grid from aqueous solution revealed that PEG–PAsp-coated magnetite nanoparticles take a cubic shape with a mean particle diameter of approximately 10 nm. The PEG–PAsp coating was observed as a layer with a thickness of approximately 5 nm, surrounding the magnetite nanoparticles. It was also observed in the TEM image that these PEG–PAsp-coated nanoparticles form clusters with a size range of 100 nm.

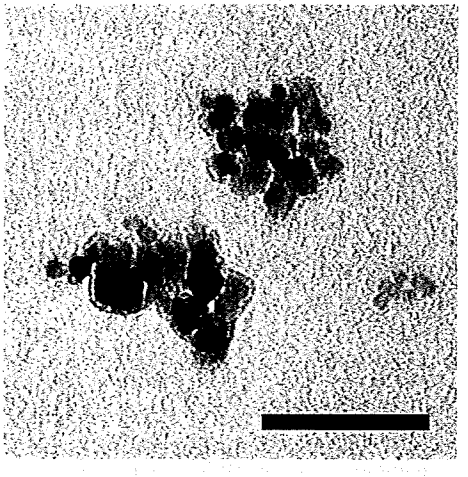

Fig. 1. TEM image of the PEG–PAsp-coated magnetite nanoparticles. Bar: 100 nm.

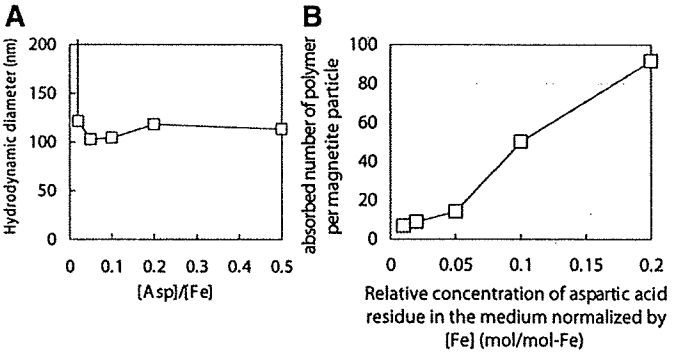

Fig. 2. Physicochemical properties of the PEG–PAsp-coated magnetite nanoparticles. (A) Hydrodynamic diameter vs. relative concentration of aspartic acid residue in the medium normalized by [Fe] (mol/mol-Fe) (=[Asp]/[Fe]), and (B) Change in the adsorbed density of PEG–PAsp on the magnetite surface estimated from TGA analysis with a bulk concentration of PEG–PAsp. Temperature = 37 °C; medium: distilled water.

The hydrodynamic diameter of these nanoparticles in aqueous medium was then measured with DLS and shown to be in the range of 100 to 120 nm with unimodal distribution, for Asp/Fe ratios ranging from 0.02–0.5. This DLS data is consistent with the cluster formation of nanoparticles indicated from TEM images. However, with a lowered Asp/Fe ratio as 0.01, the hydrodynamic diameter increased significantly (Fig. 2A). This result indicates that there is a critical surface concentration of PEG to effectively prevent the PEG–PAsp-coated magnetite nanoparticles from the agglomeration. The purified nanoparticles were stable in distilled water as 100 nm-scaled cluster at room temperature as well as at 37 °C, maintaining the initial photon count and distribution in DLS analysis for at least one month, even after the ultrafiltration to remove free PEG–PAsp possibly remained in the reactant.

The density of the PEG–PAsp block copolymer on the magnetite particle surface was estimated by TGA. Here, nanoparticles were heated in the nitrogen atmosphere to selectively vaporize the polymer fraction. Eventually, the amount of absorbed polymer on the surface of the nanoparticles was measured from the weight change by heating. The polymer density was then calculated from the TGA measurement for all the nanoparticles, assuming the cubic morphology as evidenced by microscopy and a density of 5.05 g/cm^3 for magnetite. As seen in Fig. 2B, the number of polymer strands on the nanoparticle surface was as high as 100. This data suggests that the PEG density on the magnetite nanoparticles is a little lower than that of PEGylated gold nanoparticles prepared through the surface tethering of PEG-SH [16].

3.2. The mechanism of PEG–PAsp adsorption on the magnetite nanoparticles

To confirm the formation of PEG–PAsp coating on the magnetite nanoparticles, the ζ-potential of bare and PEG–PAsp-coated magnetite nanoparticles was measured in 10 mM MOPS buffer as a function of

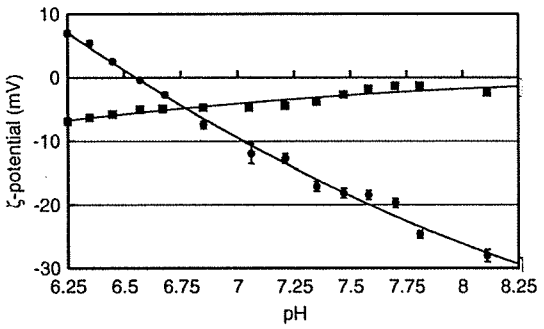

Fig. 3. Change in the ζ-potential with pH for bare (●) and PEG–PAsp-coated (■) magnetite nanoparticles. Temperature = 37 °C; medium: 10 mM MOPS buffer.

pH (Fig. 3). The isoelectric point (IEP) of the bare magnetite nanoparticles was estimated as approximately 6.6, which is consistent with the reported IEP value of iron oxide [17]. In a lower pH (below the IEP), the magnetite nanoparticle surface was protonated to result in a positive ζ-potential. Thus, in this pH range, electrostatic attraction between positively-charged magnetite nanoparticles and negatively charged PEG–PAsp is expected to occur, allowing the PEG–PAsp adsorption to the nanoparticle surface. Alternatively, the bare magnetite nanoparticles possess negative ζ-potential at physiological pH 7.4, whereas the ζ-potential shifted to the neutral value for PEG–PAsp modified nanoparticles in 10 mM MOPS buffer (pH 7.4), being consistent with the formation of a PEG shell layer. Also, these data suggest that there should be an adsorption mechanism other than simple electrostatic interaction, because magnetite has a negative ζ-potential value at pH 7.4 to induce electrostatic repulsive force against negatively charged carboxylates in PEG–PAsp. The adsorption mechanism under physiological pH was suggested to be the monodentate chelation (I) (Fig. 4) from the result of Fourier transform infrared spectroscopy [18], as explained in detail in Supplemental Text with Supplemental Fig. 1 and Supplemental Table 1.

3.3. Comparison study of the physicochemical characteristics of the PEG–PAsp- and dextran-coated magnetite nanoparticles

The MRI detection limit was compared between the PEG–PAsp- and dextran-coated magnetite nanoparticles in the field of 0.47 T at 25 °C from the relaxivity r_2, exhibiting the sensitivity of the T_2 MRI contrast agent. The dextran-coated magnetite used in this study was the one already in clinical use, Resovist®. Eventually, the relaxivity r_2 of the PEG–PAsp nanoparticle was calculated to be 138 mM^{-1} s^{-1}, the value similar to Resovist® [19].

The hydrodynamic diameter observed between the PEG–PAsp-coated and dextran-coated magnetite nanoparticles differed significantly in an NaCl-concentration-dependent manner (Fig. 5A). Although the hydrodynamic diameter of the PEG–PAsp-coated magnetite nanoparticles did not change significantly up to 3 M NaCl, indicating the appreciable stability of the PEG–PAsp-coating, that of Resovist® significantly increased even at NaCl = 0.15 M, and reached more than 1 μm at NaCl = 0.5 M, due to the drastic aggregation. Note that the PEG–PAsp-coated nanoparticles did not show any change in

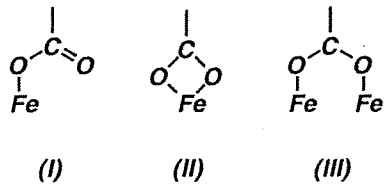

Fig. 4. Modes of carboxylate-metal complexation: monodentate (I), bidentate chelating (II), and bidentate bridging (III).

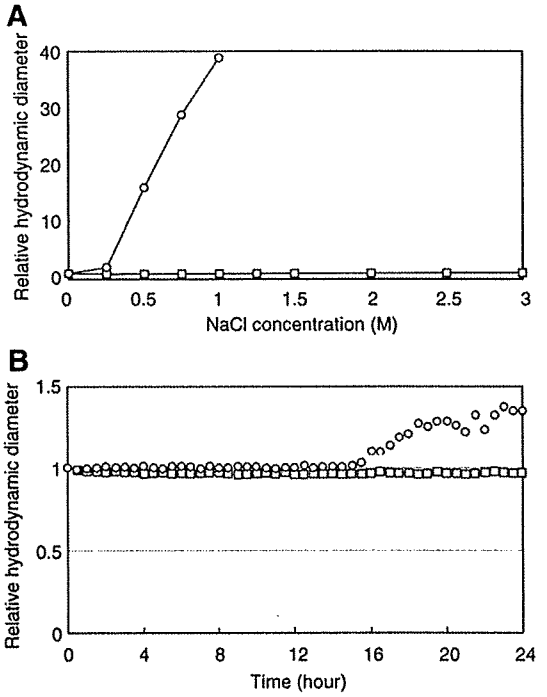

Fig. 5. NaCl concentration (A) and time (B) dependencies of the relative hydrodynamic diameter of magnetite nanoparticles, □: PEG–PAsp-coated nanoparticles, ○: dextran-coated nanoparticles (Resovist®). Fe concentration = 2 mmol/l; temperature = 37 °C; medium 10 mM Tris–HCl buffered saline (pH 7.4). 10% fetal bovine serum was contained in (B).

their size even after one month storage in 10 mM Tris–HCl buffered saline (pH 7.4, 37 °C) (data not shown).

The colloidal stability of the PEG–PAsp-coated magnetite nanoparticles in physiological conditions was also examined. We incubated them in 10 mM Tris–HCl buffered saline (pH 7.4) containing 10% fetal bovine serum at 37 °C for 24 h and measured the change of the hydrodynamic diameter (Fig. 5B). The size of the PEG–PAsp-coated magnetite nanoparticles did not obviously change during the 24-hour storage time. On the other hand, the size of Resovist® increased by the formation of aggregates after 16 h of storage time.

The stability of the PEG–PAsp-coated nanoparticles may come from the multivalent bonding between flanking carboxylic groups and the magnetite surface, as suggested by FT-IR study. These findings are consistent with a report showing that PEG-oligo(aspartic acid) block copolymer-coated iron oxide nanoparticles were stable at pH 2–11 and in 1 M NaCl, where the repeating number of aspartic acid units was 3 or more [20]. In contrast, instability of Resovist® against salt addition may be due to weak interaction between magnetite and hydroxyl groups of dextran [21].

3.4. MR imaging of experimental pancreatic cancer in vivo

The MR imaging of tumor tissue *in vivo* was then conducted by comparing PEG–PAsp- and dextran-coated magnetite nanoparticles, Resovist®. Resovist® has already been approved for clinical use as a liver-specific MRI contrast agent, due to accumulation into the reticuloendothelial system (RES) of the normal liver. Most malignant liver tumors do not contain RES cells and therefore are contrasted positive by Resovist®. A xenografted BxPC3 human pancreatic adenocarcinoma cell line in nude mice, characterized histologically by fibrosis and hypovascularity, was used as a model of intractable cancer. Recently, we reported that the administration of TGF-β inhibitor to tumor model mice significantly enhanced the intratumoral accumulation of nanoparticles encapsulating anticancer drugs [11]. Thus, we tested the effect of the i.p. administration of TGF-β

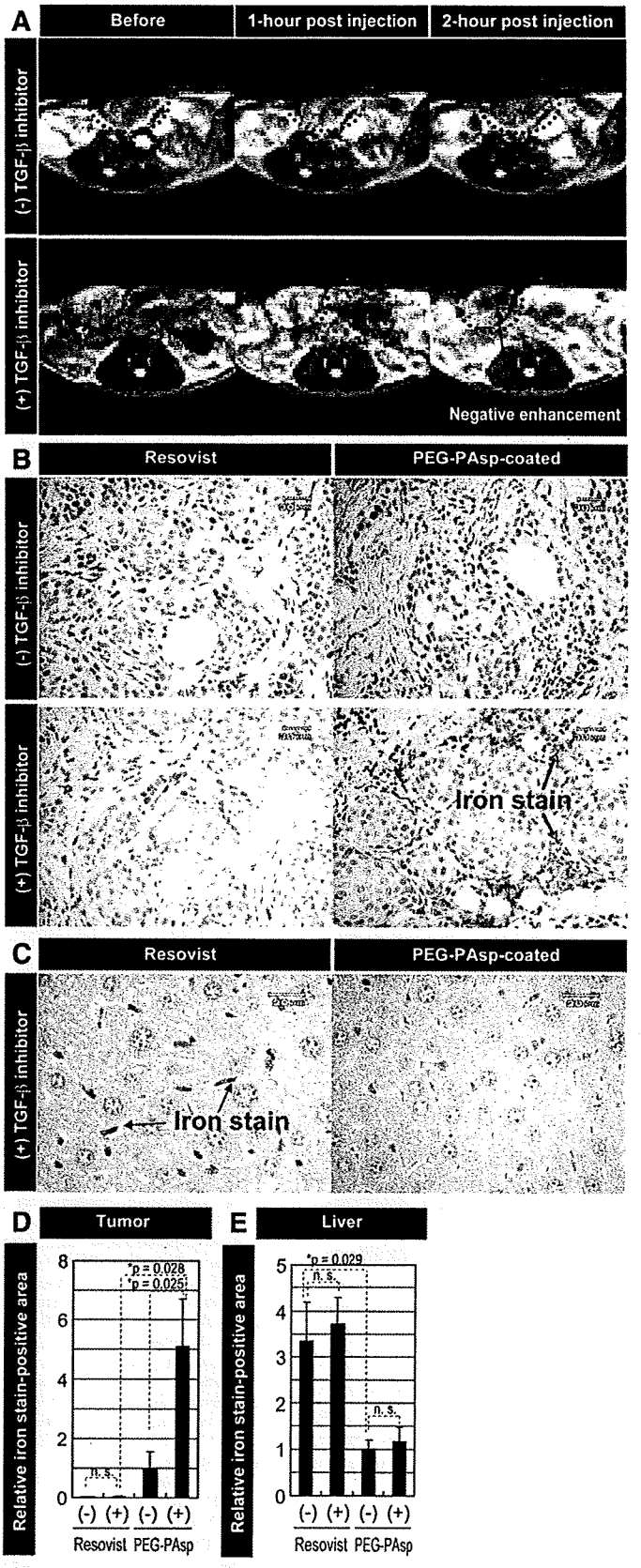

Fig. 6. MR imaging of experimental pancreatic cancer *in vivo* and the distribution of the nanoparticles in cancer and liver tissues. (A) T_2-weighted images of tumor-implanted mice (tumor sites are circled by red dotted line) at different temporal points after injection of PEG–PAsp-coated magnetite nanoparticles and TGF-β inhibitor. All images were obtained in a field strength of 4.7 T. (B) Histological sections of BxPC3 xenograft stained with Prussian blue. The distribution of Resovist® and PEG–PAsp-coated magnetite nanoparticles, at 5.5 mg/kg with and without TGF-β inhibitor at 1 mg/kg, were examined 24 h after the administration. (C) Histological sections of liver stained with Prussian blue. The distribution of Resovist® and PEG–PAsp-coated magnetite nanoparticles, at 5.5 mg/kg with TGF-β inhibitor at 1 mg/kg, was examined 24 h after the administration. (D and E) Areas of iron staining in the tumor and liver were quantified. PEG–PAsp, PEG–PAsp coated magnetite nanoparticles with (+) and without (−) inhibitor. Error bars in the graphs represent standard errors of the mean ($n = 6$), and P values were calculated by two-tailed Student's t test. n.s.: not significant.

inhibitor with the i.v. administration of Resovist® or the PEG–PAsp-coated magnetite nanoparticles on their imaging capability in size-matched xenografts of the BxPC3 cell line. Fig. 6A shows the T_2-weighted MR images of the tumors at different time periods after the intravenous administration (preinjection, and 1 and 2 h postinjection) of PEG–PAsp-coated magnetite nanoparticles with and without TGF-β inhibitor.

Resovist® failed to image the tumor even with the co-administration of TGF-β inhibitor, presumably due to the non-specific accumulation into the reticuloendothelial system [8]. In contrast, the PEG–PAsp-coated magnetite nanoparticles exhibited significant negative enhancement of signal intensity in the tumor region of T_2-weighted images when combined with TGF-β inhibitor, suggesting the accumulation of detectable amounts of the PEG–PAsp-coated magnetite nanoparticles within 2 h after injection. Therefore, the difference in behavior of these two types of magnetite nanoparticles *in vivo* had a crucial importance in achieving effective tumor accumulation for successful MR imaging.

To further verify the accumulation of iron oxide nanoparticles in the tumor, we performed Prussian blue staining of the tumor tissues to detect iron oxide, which stains blue. As shown in Fig. 6B, positive staining of the tumor for iron oxide was only obvious in the condition with PEG–PAsp-coated nanoparticles combined with the TGF-β inhibitor. Areas of iron staining in the tumor were then quantified as seen in Fig. 6D, demonstrating a significant increase in the areas of positive staining by TGF-β inhibitor treatment. The presence of iron oxide was consistent with the MRI results. Iron oxide was observed in the area rich in fibrotic components, suggesting that the administration of TGF-β inhibitor transiently increases the permeability of the tumor capillary to promote the extravasation of the PEG–PAsp-coated magnetite nanoparticles, even though the BxPC3 tumor has the characteristic of hypovascularity [11].

Lastly, we examined liver tissues from the mice treated with Resovist® or the PEG–PAsp-coated magnetite nanoparticle, with or without TGF-β inhibitor, by iron staining (Fig. 6C). Although aggregates of Resovist® accumulated in the liver, particularly in cells with smaller nuclei (presumably Kuppfer cells), far less PEG–PAsp-coated magnetite nanoparticles accumulated in the liver without aggregation. These results did not differ with or without TGF-β inhibitor, which was determined by the area of Prussian blue staining (Fig. 6E).

4. Conclusion

In conclusion, we here demonstrated the physicochemical properties of PEG–PAsp-coated magnetite nanoparticles and the feasibility of these nanoparticles as MR contrast agents for cancer diagnosis. Improving the stability of nanoparticles might be important for enabling a longer half-life in the bloodstream and a better accumulation in tumor tissue, leading to effective MR imaging with contrast agents. The neutral ζ-potential of the PEG–PAsp-coated nanoparticle may contribute to avoidance of reticuloendothelial system uptake. Formation of the stable and dense PEG layer on the magnetite surface through the anchoring of PEG–PAsp by the monodentate chelation of COO^- residues to iron atoms definitely plays a substantial role in the increased stability of the nanoparticles *in vivo*. The use of PEG–PAsp-coated magnetite nanoparticles combined with a TGF-β inhibitor could thus become a novel regime in the diagnosis of intractable cancers, including pancreatic adenocarcinoma.

Acknowledgements

The authors thank Dr James R. Christie II, The University of Tokyo, for editing the English of the manuscript. This work was supported by a Grant-in-Aid for Scientific Research from the Ministry of Education, Culture, Sports, Science and Technology (MEXT), Core Research for Evolution of Science and Technology (CREST), Japan Science and Technology Corporation (JST), and the 21st century COE program 'Human-Friendly Materials based on Chemistry' from MEXT.

Appendix A. Supplementary data

Supplementary data associated with this article can be found, in the online version, at doi:10.1016/j.jconrel.2009.06.002.

References

[1] M.R. Dreher, W. Liu, C.R. Michelich, M.W. Dewhirst, F. Yuan, A. Chilkoti, Tumor vascular permeability, accumulation, and penetration of macromolecular drug carriers, J. Natl. Cancer Inst. 98 (5) (2006) 335–344.
[2] H.A. Burris, M.J. Moore, J. Andersen, M.R. Green, M.L. Rothenberg, M.R. Modiano, M.C. Cripps, R.K. Portenoy, A.M. Storniolo, P. Tarassoff, R. Nelson, F.A. Dorr, C.D. Stephens, D.D. Von Hoff, Improvements in survival and clinical benefit with gemcitabine as first-line therapy for patients with advanced pancreas cancer: a randomized trial, J. Clin. Oncol. 15 (6) (1997) 2403–2413.
[3] D.V. Sahani, Z.K. Shah, O.A. Catalano, G.W. Boland, W.R. Brugge, Radiology of pancreatic adenocarcinoma: current status of imaging, J. Gastroenterol. Hepatol. 23 (1) (2008) 23–33.
[4] D.L. Huber, Synthesis, properties, and applications of iron nanoparticles, Small 1 (5) (2005) 482–501.
[5] R. Weissleder, G. Elidonzo, J. Wittenberg, C.A. Rabito, H.H. Bengele, L. Josephson, Ultrasmall superparamagnetic iron oxide: characterization of a new class of contrast agents for MR imaging, Radiology 175 (2) (1990) 489–493.
[6] M. Lewin, N. Carlesso, C.H. Tung, X.W. Tang, D. Cory, D.T. Scadden, R. Weissleder, Tat peptide-derivatized magnetic nanoparticles allow *in vivo* tracking and recovery of progenitor cells, Nat. Biotechnol. 18 (4) (2000) 410–414.
[7] Y.W. Jun, J.H. Lee, J. Cheon, Chemical design of nanoparticle probes for high-performance magnetic resonance imaging, Angew. Chem. Int. Ed. 47 (28) (2008) 5122–5135.
[8] D.D. Stark, R. Weissleder, G. Elizondo, et al., Superparamagnetic iron oxide: clinical application as a contrast agent for MR imaging of the liver, Radiology 168 (2) (1988) 297–301.
[9] T. Neuberger, B. Schöpf, H. Hofmann, M. Hofmann, B. von Rechenberg, Superparamagnetic nanoparticles for biomedical applications: possibilities and limitations of a new drug delivery system, J. Magn. Mater. 293 (1) (2005) 483–496.
[10] M. Kumagai, Y. Imai, T. Nakamura, Y. Yamasaki, M. Sekino, S. Ueno, K. Hanaoka, K. Kikuchi, T. Nagano, E. Kaneko, K. Shimokado, K. Kataoka, Iron hydroxide nanoparticles coated with poly(ethylene glycol)–poly(aspartic acid) block copolymer as novel magnetic resonance contrast agents for *in vivo* cancer imaging, Colloids Surf. B: Biointerfaces 56 (1–2) (2007) 174–181.
[11] M.R. Kano, Y. Bae, C. Iwata, Y. Morishita, M. Yashiro, M. Oka, T. Fujii, A. Komuro, K. Kiyono, M. Kaminishi, K. Hirakawa, Y. Ouchi, N. Nishiyama, K. Kataoka, K. Miyazono, Improvement of cancer-targeting therapy, using nanocarriers for intractable solid tumors by inhibition of TGF-β signaling, Proc. Natl. Acad. Sci. U. S. A. 104 (9) (2007) 3460–3465.
[12] Y. Matsumura, H. Maeda, A new concept for macromolecular therapeutics in cancer-chemotherapy-mechanism of tumoritropic accumulation of proteins and the antitumor agent SMANCS, Cancer Res. 46 (12) (1986) 6387–6392.
[13] N. Nishiyama, M. Yokoyama, T. Aoyagi, T. Okano, Y. Sakurai, K. Kataoka, Preparation and characterization of self-assembled polymer-metal complex micelle from cis-dichlorodiammineplatinum(II) and poly(ethylene glycol)–poly(alpha,beta-aspartic acid) block copolymer in an aqueous medium, Langmuir 15 (2) (1999) 377–383.
[14] E. Fukushima, S.B.W. Roeder (Eds.), Experimental pulse NMR: a nuts and bolts approach, Addison-Wesley, Reading, Mass, 1981, pp. 28–35.
[15] A.J.S. MacFadzean, L.J. Davis, Iron-staining erythrocytic inclusions with especial reference to acquired haemolytic anaemia, Glasgow Med. J. 28 (1947) 237–279.
[16] S. Takae, Y. Akiyama, H. Otsuka, T. Nakamura, Y. Nagasaki, K. Kataoka, Ligand density effect on biorecognition by PEGylated gold nanoparticles: regulated interaction of RCA120 lectin with lactose installed to the distal end of tethered PEG strands on gold surface, Biomacromolecules 6 (2) (2005) 818–824.
[17] L. Cromières, V. Moulin, B. Fourest, E. Giffaut, Physico-chemical characterization of the colloidal hematite/water interface: experimentation and modeling, Colloids Surf., A. Physicochem. Eng. Asp. 202 (1) (2002) 101–115.
[18] L.J. Kirwan, P.D. Fawell, W. van Bronswijk, In situ FTIR-ATR examination of poly (acrylic acid) adsorbed onto hematite at low pH, Langmuir 19 (14) (2003) 5802–5807.
[19] Y.X.J. Wang, S.M. Hussain, G.P. Krestin, Superparamagnetic iron oxide contrast agents: physicochemical characteristics and applications in MR imaging, Eur. Radiol. 11 (11) (2001) 2319–2331.
[20] S.R. Wan, J.S. Huang, M. Guo, H. Zhang, Y. Cao, H. Yan, K. Liuet, Biocompatible superparamagnetic iron oxide nanoparticle dispersions stabilized with poly (ethylene glycol)oligo(aspartic acid) hybrids, J. Biomed. Mater. Res. A 80A (4) (2007) 946–954.
[21] C.W. Jung, Surface-properties of superparamagnetic iron-oxide MR contrast agents — ferumoxides, ferumoxtran, ferumoxsil, Magn. Reson. Imaging 13 (5) (1995) 675–691.

Published online 22 February 2009

Nucleic Acids Research, 2009, Vol. 37, No. 7 ***2249–2263***
doi:10.1093/nar/gkp066

Massive transcriptional start site analysis of human genes in hypoxia cells

Katsuya Tsuchihara[1], Yutaka Suzuki[2,*], Hiroyuki Wakaguri[2], Takuma Irie[2], Kousuke Tanimoto[2], Shin-ichi Hashimoto[3], Kouji Matsushima[3], Junko Mizushima-Sugano[2,4], Riu Yamashita[5], Kenta Nakai[5], David Bentley[6], Hiroyasu Esumi[1] and Sumio Sugano[2]

[1]Cancer Physiology Project, Research Center for Innovative Oncology, National Cancer Center Hospital East: 6-5-1 Kashiwanoha, Kashiwa, Chiba 277-8577, [2]Graduate School of Frontier Sciences, the University of Tokyo: 5-1-5 Kashiwanoha, Kashiwa, Chiba 277-8562, [3]Graduate School of Medicine, the University of Tokyo: 7-3-1 Hongo, Bunkyokyu, Tokyo 113-0033, [4]Laboratory of Molecular Virology, Kitasato Institute for Life Sciences, Kitasato University: 5-9-1 Shirokane, Minatoku, Tokyo 108-8641, [5]Institute of Medical Science, the University of Tokyo: 4-6-1 Shirokenedai, Minatoku, Tokyo 108-8639, Japan and [6]Illumina, Inc: 25861 Industrial Boulevard Hayward, CA 94545, USA

Received October 3, 2008; Revised January 20, 2009; Accepted January 22, 2009

ABSTRACT

Combining our full-length cDNA method and the massively parallel sequencing technology, we developed a simple method to collect precise positional information of transcriptional start sites (TSSs) together with digital information of the gene-expression levels in a high throughput manner. We applied this method to observe gene-expression changes in a colon cancer cell line cultured in normoxic and hypoxic conditions. We generated more than 100 million 36-base TSS-tag sequences and revealed comprehensive features of hypoxia responsive alterations in the transcriptional landscape of the human genome. The features include presence of inducible 'hot regions' in 54 genomic regions, 220 novel hypoxia inducible promoters that may drive non-protein-coding transcripts, 191 hypoxia responsive alternative promoters and detailed views of 120 novel as well as known hypoxia responsive genes. We further analyzed hypoxic response of different cells using additional 60 million TSS-tags and found that the degree of the gene-expression changes were different among cell lines, possibly reflecting cellular robustness against hypoxia. The novel dynamic figure of the human gene transcriptome will deepen our understanding of the transcriptional program of the human genome as well as bringing new insights into the biology of cancer cells in hypoxia.

INTRODUCTION

Aberrantly growing cancer cells in solid tumors frequently encounter a shortage of blood flow, which leads to insufficient oxygen supply. Tumor cells adapt themselves to such hypoxic microenvironment by shifting their ATP production metabolism from oxidative phosphorylation to anaerobic glycolysis, and by enhancing glucose intake. Tumor cells also induce angiogenesis to acquire additional blood supplies. Such adaptations are supposed to be essential in survival as well as malignant transformation of tumor cells *in vivo* (1,2). During this series of events, transcriptional regulation plays a pivotal role. It has been well documented that hypoxia inhibits proteasomal degradation of α subunits of hypoxia inducible factors (HIF1α and HIF2α). Stabilized subunits translocate from the cytoplasm into the nucleus and form a heterodimer complex with HIF1β. HIF complexes transactivate various downstream genes, such as the genes encoding glycolytic enzymes, glucose transporters, the enzymes eradicating organic acids and VEGF which induces angiogenesis. However, the specific function of each isoform of the subunits remains unclear. Meanwhile, 'HIF-independent' regulation of hypoxia-inducible genes has also been documented (3,4). Thus, the current view of hypoxic versatility in transcriptome programs in cancer cells is still far from comprehensive. A bird's eye view on what range of genes are induced in what manner still remains mostly elusive. Although some genome-wide expression profiles using microarrays have been reported, they represent mere collective information of the fold inductions of the individual genes (5–9). In this regards, we believed that information

*To whom correspondence should be addressed. Tel/Fax: +81 4 7136 3607; Email: ysuzuki@k.u-tokyo.ac.jp

about exact positions of transcriptional start sites (TSSs) and absolute levels of the transcriptions starting from them would lead to more comprehensive understandings.

Several methods based on cDNA analysis have been developed for large-scale identification of TSSs (10–13). We have also developed a method to selectively replace the cap structure of the mRNA with a synthetic oligo, which we named the oligo-capping method (11). By sequencing 1.8 million cDNAs isolated from oligo-cap cDNA libraries from various kinds of human cells and tissues (14), we have collected the positional information of the TSS and analyzed putative proximal promoter regions (15,16). We, as well as another research group in RIKEN, have further improved the efficacy of this approach by combining the cap-selection method with the SAGE method (17,18). In these methods, 5′-ends of full-length cDNAs were concatenated, so that 10–15 20-base long 5′-end tag sequences could be identified by single-pass sequencing. By intensive analysis of CAGE-tag libraries in humans and mice, the FANTOM consortium reported a first glimpse of the transcription landscape of mammalian genomes (19,20). However, such an overview of the TSSs has been obtained from collective analysis of various cell types and tissues, for each of which the data coverage still remains scarce. Therefore, it does not represent the actual transcriptional landscape in any given cell type. Besides, it has been suggested recently that mammalian genes seem to utilize multiple alternative promoters very frequently, which enable a single locus to encode functionally distinct proteins, thereby serving as a molecular basis for realizing multifaceted use of a limited number of human genes (21,22). Nonetheless, the depth of the analysis has not reached the level of these alternative promoters, whose expression levels are often low and limited to particular cell types or cellular environments.

Recently developed massively parallel sequencing technologies have provided a potential mean to further improve the throughput of TSS identification. For example, Illumina GA sequencer (23) can sequence 10–30 million sequences per run. Although the read length which this sequencer can generate is short (currently up to 36 bases), it is sufficient to uniquely determine the precise positions of TSS. By combining oligo-capping method with the Illumina GA technology, we developed a simple method to collect information of the TSS together with the digital data of the expression levels of the transcripts. Here we show this approach enabled us to see the genome wide transcriptional landscape in response to hypoxia in a human colorectal cancer cell line.

MATERIALS AND METHODS

Cell culture and RNA interference

Human cell line, DLD-1 cells, was purchased from American Type Culture Collection (ATCC number: CCL-221). Cells were maintained in Dulbecco's modified Eagle's medium (DMEM) (Invitrogen) supplemented with 10% fetal calf serum, 4.5 g/l glucose, and antibiotics. RNA interference was accomplished by transfecting DLD-1 cells with the specific siRNA. HIF1A and EPAS1 (HIF2A)-targeting siRNA pool and non-silencing siRNA pool were purchased from Dharmacon. Short oligo-RNAs were transfected using Dharmafect 1 transfection reagent (Dharmacon) as recommended by the manufacturer. For constructing other TSS-libraries, HEK293, MCF7 and TIG3 cells (ATCC number: CRL-1573, ATCC number: HTB-22 and Japan Cell Resource Bank number: JCRB0506, respectively) were cultured in standard conditions and were subjected to the hypoxic shocks in a similar manner.

Oligo-capping and massively parallel sequencing by Illumina GA Sequencer

Six million DLD-1 cells were seeded 24 h before transfection. The cells transfected with HIF-targeting and control siRNA were cultured in 21% O_2 and 5% CO_2 at 37°C for 24 h followed by incubation in 21% O_2 or 1% O_2 and 5% CO_2 for 24 h. Cells were harvested and RNA was extracted using RNeasy (Qiagen). Two hundred microgram of the obtained total RNA was subjected to oligo-capping with some modifications from the original protocol; namely after the successive treatment of the RNA with 2.5 U BAP (TaKaRa) at 37°C for 1 h and 40 U TAP (Ambion) at 37°C for 1 h, the BAP-TAP-treated RNAs were ligated with 1.2 μg of RNA oligo (5′-AAUGAUACGGCGACCACCGAGAUCUACACU CUUUCCCUACACGACGCUCUUCCGAUCUGG-3′) using 250 U T4 RNA ligase (TaKaRa) at 20°C for 3 h. After the DNase I treatment (TaKaRa), polyA-containing RNA was selected using oligo-dT powder (Collaborative). First strand cDNA was synthesized from 10 pmol of random hexamer primer (5′-CAAGCAGAAGACGGCA TACGANNNNNNC-3′) using Super Script II (Invitrogen) by incubating at 12°C for 1 h and at 42°C overnight. Template RNA was degraded by alkarine treatment. For PCR, one-fifth of the first strand cDNAs were used as the PCR template. Gene Amp PCR kits (PerkinElmer) were used with the PCR primers 5′-AAT GATACGGCGACCACCGAG-3′ and 5′-CAAGCAGA AGACGGCATACGA-3′ under the following reaction conditions: 15 cycles of 94°C for 1 min, 56°C for 1 min and 72°C for 2 min. The PCR fragments were size fractionated by 12% polyacrylamide gel electrophoresis and the fraction of 150–250 bp was recovered. The quality and quantity of the obtained single-stranded first strand cDNAs were assessed, again, using BioAnalyzer (Agilent).

One nanogram of the size fractionated cDNA was used for the sequencing reactions with the Illumina GA. 15 000–20 000 clusters were generated per 'tile' and 36 cycles of the sequencing reactions were performed according to the manufacturer's instructions.

Data processing

The obtained sequences were mapped onto human genomic sequences (hg18 as of UCSC Genome Browser; http://genome.ucsc.edu/) using the sequence alignment program Eland. Unmapped or redundantly mapped sequences were removed from the dataset. For uniquely mapped sequences, relative positions to RefSeq genes were calculated based on the respective genomic coordinates.